

Correspondence between excited energy eigenstates and local minima of the energy landscape in quantum spin systems

Yang Wei Koh 

Institute of Innovative Research, Tokyo Institute of Technology, Nagatsuta-cho, Midori-ku, Yokohama 226-8503, Japan



(Received 27 December 2022; revised 4 June 2023; accepted 7 June 2023; published 16 June 2023)

The quantum-classical correspondence between local minima on the classical energy landscape and excited eigenstates in the energy spectrum is studied within the context of many-body quantum spin systems. In mean-field approximations of a quantum problem, one usually focuses on attaining the global minimum of the resulting energy function, while other minimum solutions are usually ignored. For frustrated systems, a strict distinction between global and local minimum is often not tenable since first-order-type transitions can interchange the roles played by two different minima. This begs the question of whether there is any physical interpretation for the local minima encountered in mean-field approximations of quantum systems. We look at the problem from the perspective of quantum spin systems. Two models are studied, a frustrated model with quenched disorder and a pure system without frustration. Accurate classical energies of the minima are compared with the full spectrum of energy levels, allowing us to search for signs of correspondence between them. It is found that the local minima can generally be interpreted as excited energy eigenstates. Instances of spurious minima are also reported.

DOI: [10.1103/PhysRevB.107.224203](https://doi.org/10.1103/PhysRevB.107.224203)

I. INTRODUCTION

The study of excited energy eigenstates is recently receiving some interest in the context of many-body quantum spin systems [1,2]. In quantum optimization algorithms, for instance, excited states appear as suboptimal solutions when the system falls out of equilibrium after undergoing diabatic or thermal transition [3]. Apart from practical issues associated with applications, there are also some basic questions regarding the identity or interpretation of excited states in quantum spin systems, particularly in the presence of frustration. On one hand, from a classical perspective, the defining feature of frustration is a rugged energy landscape exhibiting many minima, with metastable states residing in the local minima. On the other hand, from a purely quantum mechanical point of view, energies are eigenvalues of the Hamiltonian operator, with frustration manifested through the statistics of level spacings or eigenvector amplitudes [4,5]. The question that arises naturally is whether there is a correspondence between the quantum and classical excited energy states. In other words, is there a physical interpretation for the local minima frequently encountered in semiclassical treatments of quantum spin Hamiltonians [6], or are these minima artifacts of the mathematical treatment.

Let us be more precise about what we mean by the term classical energy. The Hartree-Fock wave function $|0\rangle$ is defined as the direct product of single-spin states [6,7]

$$|0\rangle = \prod_{i=1}^N \begin{pmatrix} \alpha_i \\ \beta_i \end{pmatrix}, \quad (1)$$

where α_i and β_i are the spinor components of the i th spin in the basis where its z -directional Pauli matrix σ_i^z is diagonal, and

N is the total number of spins. Normalization of $|0\rangle$ requires that $\alpha_i^2 + \beta_i^2 = 1$ for all i . By the classical energy landscape of a Hamiltonian operator H , we mean the expectation value $\langle 0|H|0\rangle$, which is an N -dimensional function of the spin variables α_i [8]. Traditionally, Hartree-Fock approximation gives an estimation of the ground-state energy of H by minimizing $\langle 0|H|0\rangle$ with respect to α_i :

$$E_0^{\text{HF}}(H) = \min_{\{\alpha_i\}} \langle 0|H|0\rangle. \quad (2)$$

An implicit assumption is that there is only one minimum on the classical energy surface, so we can unambiguously identify the Hartree-Fock energy E_0^{HF} with the ground-state energy E_0 . When there is quenched disorder in H , however, there can be many local minima on the energy surface. This poses the question of whether evaluating the Hartree-Fock energy at the local minima is meaningful as well, and if these local minima energies correspond to actual energy levels in the quantum spectrum.

There are many previous studies on local minima in disordered quantum spin systems. The nature of the transition between the paramagnetic and spin-glass phases has been investigated in a variety of models ranging from the Heisenberg model [9], the Sherrington-Kirkpatrick model [10–15], rotor models [16,17], to p -spin models [18–21]. A wide range of techniques such as perturbative expansion [10], replica method [11,13,14,20,21], quantum Monte Carlo simulations [12], Landau effective-action functional [17], and $1/p$ expansion [18] have also been employed to study these transitions. For a summary of some of these methods and their results, see Ref. [15]. The so-called “dynamical effects” induced by quantum fluctuations on the spin-glass phase have also been studied in some models at both finite and zero temperatures

using a variety of techniques [22–25]. In most of these earlier works, one usually performs an average over the quenched disorder using the replica method. On the other hand, in the approach via the quantum Thouless-Anderson-Palmer (TAP) equations [26–28], one can choose to study the system under a specific realization of disorder. Compared to the replica approach, this viewpoint offers a more intuitive picture of the glassy phase in the form of a rugged free-energy landscape, with the exponentially many TAP solutions as the local minima. The general formalism of the quantum TAP approach has been developed in Ref. [28], and applied to the spherical p -spin model to obtain the generic phase diagram for quantum spin glasses. The Hartree-Fock method we adopted above has some similarities with the quantum TAP approach, but also some differences. Like the TAP approach, the Hartree-Fock method works with specific realizations of quenched disorder, and the scenario of a rugged energy landscape emerges as well. In the case of some simple mean-field models (e.g., the ferromagnetic model in Appendix B), their mean-field equations are also similar. On the other hand, while the quantum TAP approach is applicable at finite temperatures, the Hartree-Fock method is usually only used for zero-temperature calculations. The kinds of approximation which are involved in the two methods are also quite different. The TAP equations become exact in the thermodynamic and infinite-dimension limit, whereas for the Hartree-Fock approximation, corrections in the form of correlation energy (discussed below) must be incorporated regardless of system size or dimension.

Another way of studying disordered quantum spin systems is from the perspective of quantum chaos [4,5,29–36]. In this approach, one mainly focuses on purely quantum mechanical attributes such as level statistics [4,29,31–33], level dynamics [30], eigenstate amplitudes distribution [5,29], and entanglement [31], rather than on the local minima. Also, many works in the literature are devoted to disordered spin chains [4,5,29,31] or two-dimensional models [31–33], in which the spin-glass phase is usually considered to be absent. An exception is an early paper by Georgeot and Shepelyansky which showed how the level spacing distribution changes between Poisson and Wigner-Dyson as one tunes the strength of the transverse field in the quantum Sherrington-Kirkpatrick model [34]. Interestingly in this work, the relation between the statistics of the level spacings and the spin-glass phase is not very straightforward because the distribution reverts back to Poisson (i.e., nonchaotic) when deep within the glassy regime. Recently, there is growing interest in the relationship between the spin-glass phase and quantum chaos, for instance, from the viewpoints of Lyapunov exponent [35] and spectral form factor [36].

A slightly different angle to view and perhaps bring together these two perspectives is offered by recent discussions on many-body localization delocalization (MBLD) in quantum spin glasses [37–39], where extensive studies on the energy levels and eigenstates of such systems revealed a transition between localized and delocalized phases reminiscent of many-body localizations observed in spin chains [40–45]. However, as noted by Baldwin *et al.* in Ref. [38], the mechanisms underlying the transitions are quite different between mean-field and chain models, with large energy barriers play-

ing the dominant role in MBLD. The authors also pointed out a possible relation between the mobility edge in MBLD and the dynamical transition ushering a system into the rugged free-energy phase (cf. the quantum TAP approach Ref. [28]). As in studies on quantum chaos, however, in MBLD one focuses mainly on quantum attributes such as level spacings or entanglement entropy, so the intuitive role played by local minima in the localization mechanism is, nevertheless, not very transparent.

This work is in part an effort to bridge and find a relationship between these two different points of view, namely, the classical description in terms of local minima versus the quantum picture based on energy levels and eigenstates. In particular, we are focusing on a specific aspect, namely, to see if a correspondence can be established between the energy levels in the quantum spectrum and the energies of the classical local minima. In many of the works reviewed above, one adopts a statistical stance and looks at the general properties of a system via “bulk” quantities such as the average free energy or the level statistics. Here, on the other hand, our approach is to match pairs of quantum and classical states together individually. Overall, we were able to find evidences of a quantum-classical correspondence between the two. More specifically, the correspondence yields a picture of highly excited eigenstates which are largely confined around the classical local minima. We stress that it is not our aim here to address the challenging issues reviewed above (i.e., quantum chaos and MBLD). Nonetheless, we feel that our work might still contribute some insights into those questions.

Apart from theoretical considerations, such a correspondence relation may also be useful in practical scenarios. In quantum annealing and optimization [3], for instance, a phenomenon known as “freezing” where the system gets stuck in a suboptimal Boltzmann distribution, thereby failing to attain the global minimum solution, has been observed both in numerical simulations [46] and experimentally on the D -wave machine [47]. Due to the high dimensionality of the Hilbert space involved, quantum annealing processes are usually interpreted in terms of a classical trajectory on an approximate mean-field energy landscape. In Refs. [46,47], freezing has been attributed to trappings by local minima on such energy surfaces. Interestingly, the situation here is somewhat the opposite of quantum chaos and MBLD discussed above. Whether and how the local minima, based on a mean-field picture, represent the actual quantum states of the system is not very clear. A closely related issue concerns the role played by tunneling in quantum annealing, particularly in the D -wave machine [47,48]. In these works, tunneling is analyzed with the assumption that the system makes a transition from one local minimum to another. On the other hand, as will be demonstrated in Sec. IV, an excited energy eigenstate is sometimes formed by superposing several local minima together. Hence, a more accurate analysis of tunneling in frustrated systems might need to account for such multiple-minima effects. These considerations may play an important role when, say, improving the efficiencies of quantum optimization algorithms.

A second contribution of this work concerns the numerical calculation of classical energy. In the preceding discussion, we have interpreted the classical energy to be the Hartree-Fock

energy. However, Hartree-Fock approximation is sometimes not precise enough to enable one to perform the quantum-classical correspondence mentioned above. In particular, in the high-energy regime where the local minima reside, the spectral lines are quite closely spaced and so the classical energy needs to be relatively close to the appropriate energy eigenvalue in order for one to see their correspondence. The way to improve upon Hartree-Fock approximation is to incorporate the correlation energy via coupled-cluster theory [49,50]. In standard coupled-cluster theory, one performs a Hausdorff expansion of the transformed Hamiltonian

$$e^{-T} H e^T = H + [H, T] + \frac{1}{2} [[H, T], T] + \frac{1}{3!} [[[H, T], T], T] + \dots, \quad (3)$$

where T is the excitation operator generating multispin excitations when acting on the Hartree-Fock wave function [51]. The combination of Hartree-Fock approximation and coupled-cluster theory has traditionally been used for electronic structure calculations in quantum chemistry [49,50], and subsequently also in condensed matter physics to treat systems such as the Hubbard model [52]. In these fermionic systems, the models are expressed in terms of creation and annihilation operators c^\dagger and c , and the expansion (3) terminates after a finite number of terms due to the anticommutator relation $\{c, c^\dagger\} = 1$. On the other hand, in spin systems the Pauli matrices σ^α ($\alpha = x, y, z$) obey the relation $[\sigma^\alpha, \sigma^\beta] = 2i\epsilon_{\alpha\beta\gamma}\sigma^\gamma$ ($\epsilon_{\alpha\beta\gamma}$: Levi-Civita symbol) where a commutator between two matrices produces a third one, unlike the case of fermions. A naive evaluation of Eq. (3) for spin systems is therefore not guaranteed to terminate. The formulation of a finite (i.e., terminating) Hausdorff expansion in terms of three operators σ^\pm and σ^z was pioneered by Roger and Hetherington [53], and coupled-cluster theory has since been applied on a variety of spin systems [53–61]. However, for an arbitrary Hamiltonian with quenched disorder, the evaluation of this expansion is in general still quite involved, requiring the use of a pattern-matching computer-algebra program just for setting up the coupled-cluster equations alone [56,57,62].

In this work, we propose a different way of formulating coupled-cluster theory for spin systems that circumvents the Hausdorff expansion altogether. For certain types of mean-field systems, our approach simplifies the process of deriving the coupled-cluster energy and equations. Consider operators of the form

$$J_\alpha(\mathbf{a}) = \sum_{i=1}^N a_i \sigma_i^\alpha, \quad (4)$$

where σ_i^α is the α -directional Pauli matrix of the i th spin, and a_i is the i th component of the N -dimensional vector \mathbf{a} . Let us restrict ourselves to models whose H and T can be expressed in terms of polynomials of operators like $J_\alpha(\mathbf{a})$. The transformation $e^{-T} H e^T$ can then be evaluated without performing the expansion (3) explicitly. To illustrate, consider a two-body operator $T = \frac{1}{2} [J_\alpha(\mathbf{a})]^2$. We generalize the Hubbard-Stratonovich transformation to operators

$$e^{\frac{1}{2} [J_\alpha(\mathbf{a})]^2} = \int_{-\infty}^{\infty} \frac{dm}{\sqrt{2\pi}} \exp \left[-\frac{1}{2} m^2 + m J_\alpha(\mathbf{a}) \right]. \quad (5)$$

It is seen that the quadratic operator $[J_\alpha(\mathbf{a})]^2$ has been “linearized” on the right side of Eq. (5) by introducing the random Gaussian field m . It is then straightforward to evaluate individual terms in $e^{-T} H e^T$ by applying the formula

$$e^{-\lambda J_\beta(\mathbf{b})} J_\alpha(\mathbf{a}) e^{\lambda J_\beta(\mathbf{b})} = J_\alpha(\mathbf{c}) + i \epsilon_{\alpha\beta\gamma} J_\gamma(\mathbf{d}), \quad (6)$$

where $c_i = a_i \cosh(2\lambda b_i)$, $d_i = a_i \sinh(2\lambda b_i)$, λ is a parameter, and $\epsilon_{\alpha\beta\gamma}$ is the Levi-Civita symbol. Equations (5) and (6) in effect achieve the same purpose as the Hausdorff expansion (3). After they have been applied, the setting up of the coupled-cluster energy and equations is straightforward and will be detailed in Sec. II. The above approach simplifies some of the mathematical derivations encountered in coupled-cluster theory.

As mentioned, coupled-cluster theory has been used to study a variety of spin systems. Its performance in spin chains [53–55] and various two-dimensional lattices [53–57,59,61] has been benchmarked and examined in considerable detail. These studies have shown that coupled-cluster theory is an accurate and efficient numerical method for calculating the ground-state properties of low-dimensional lattice spin models. On the other hand, its performance in fully connected models, especially in the presence of quenched disorder, has received lesser attention. It is the secondary objective of this work to assess the feasibility of coupled-cluster theory for treating mean-field systems. We study models whose Hamiltonian matrix is amenable to exact diagonalization, thereby allowing us to benchmark the results of coupled-cluster calculations. We also apply coupled-cluster theory to local minima on the Hartree-Fock energy surface to see if the energies of excited states are obtainable from local minima. We found that at large system sizes, coupled-cluster theory is effective and gives significant improvement upon Hartree-Fock approximation. However, at small system size, and particularly when quenched disorder is present, we encountered situations whereby there are no physically valid solutions to the coupled-cluster equations. Overall, our assessment of the effectiveness of the coupled-cluster method for mean-field models remains inconclusive. In particular, the question of its performance in disordered systems when the number of spins is large remains open and requires further study.

In this paper, we address the questions outlined above by case studying two models. The rest of the paper is organized as follows. Section II presents the random field formulation of coupled-cluster theory at the level of singles-doubles approximation (CCSD). Section III is on a model without frustration, the cubic model under transverse field and antiferromagnetic interactions. This is a simple system, chosen because its energy surface exhibits just one local minimum. After defining the model and reviewing its phase diagram and ground-state energy, we focus our attention on the local minimum. The main result here is that in the quantum spectrum, a series of consecutive energy levels form an envelope of avoided crossings, and the energy of the local minimum lies very closely on this envelope. Hence, the quantum-classical correspondence is established between the local minimum and this “secondary” structure, rather than with any particular energy level. We then examine the quantum and classical wave functions along the envelope to ascertain the correspondence. Section IV is on the

Hopfield model in transverse field. This is a frustrated system exhibiting multiple local minima on its energy surface. After a brief review of the model, we study the rugged structure of the energy landscape in some detail. This is followed by examination of the energy eigenvalues and eigenfunctions, where we found quantum states being localized in the energy basins of local minima. Lastly, Sec. V summarizes and concludes the paper.

To aid in the flow of our presentation, some technical materials are deferred to the Appendixes. Appendix A gives a list of CCSD formulas used in this paper. Appendix B applies CCSD to a simple model, the ferromagnetic model in transverse field, illustrating in some detail the implementation of the method. Appendix C presents the wave functions of the classical approximations, which will be employed when ascertaining quantum-classical correspondence. The reader is referred to these supplements for technical details.

II. RANDOM FIELD FORMULATION OF COUPLED-CLUSTER THEORY

In this section, we present the random field formulation of coupled-cluster theory. We illustrate our method by outlining the main steps in the derivation of $\langle 0|e^{-T} J_x e^T |0\rangle$, which is one of the terms (the transverse field) in the coupled-cluster energy. We then state the results for the other terms in Appendix A. The notation J_α denotes $J_\alpha(\mathbf{a})$ with all components of \mathbf{a} set to unity. The coupled-cluster energy and equations for the models studied in this paper are obtained by combining terms listed there. For general aspects of coupled-cluster theory, the reader is referred to Refs. [49,50].

In this paper, we employed the singles-doubles approximation in the coupled-cluster expansion (CCSD). The excitation operator T in Eq. (3) is truncated at the second-order term, and the coupled-cluster energy is no longer exact. Previous works have shown CCSD to be an economic approximation to try when approaching any new model. As we shall demonstrate in later sections, it leads to very accurate results when the system size is large.

For the models we considered, T can be written as

$$T^{\text{SD}} = y \sum_{i=1}^N f_i + \frac{1}{2} \left(\sqrt{w} \sum_{i=1}^N f_i \right)^2. \quad (7)$$

The operator $f_i = -i\sigma_i^y$ flips the i th spinor $\begin{pmatrix} \alpha \\ \beta \end{pmatrix}$ (α, β real). The variables y and w (> 0) are, respectively, the amplitudes for singles and doubles excitations, and they are determined by solving the CCSD equations. Applying Eq. (5) followed by Eq. (6), one has

$$e^{-T^{\text{SD}}} J_x e^{T^{\text{SD}}} = \int \mathcal{D} e^{(i\bar{m}+m)\sqrt{w} \sum_i f_i} (J_x \cos 2z + J_z \sin 2z), \quad (8)$$

where $\int \mathcal{D} = \int_{-\infty}^{\infty} \int_{-\infty}^{\infty} \frac{dm d\bar{m}}{2\pi} e^{-\frac{1}{2}(m^2 + \bar{m}^2)}$ and $z = y + m\sqrt{w}$. Before taking the expectation value of Eq. (8) with respect to the Hartree-Fock wave function $|0\rangle = \begin{pmatrix} \alpha \\ \beta \end{pmatrix}^N$, it is convenient to define

$$b_1 = \cosh \sqrt{w}(im - \bar{m}), \quad b_2 = \sinh \sqrt{w}(im - \bar{m}) \quad (9)$$

and

$$\begin{aligned} P_1 &= 2\alpha\beta + (\alpha^2 - \beta^2)(ib_2/b_1) \\ P_2 &= 2\alpha\beta(ib_2/b_1) - (\alpha^2 - \beta^2). \end{aligned} \quad (10)$$

We then have

$$\langle 0|e^{-T^{\text{SD}}} J_x e^{T^{\text{SD}}} |0\rangle = N \int \mathcal{D} b_1^N (P_1 \cos 2z - P_2 \sin 2z). \quad (11)$$

To integrate out the random fields m and \bar{m} , we use the identities

$$\begin{aligned} \int \mathcal{D} b_1^N \left(\frac{ib_2}{b_1} \right)^n \cos \mu z &= i^n e^{-\frac{\mu^2 w}{2}} \cosh^N(\mu w) \tanh^n(\mu w) \\ &\times \left[\frac{(-1)^n e^{i\mu y} + e^{-i\mu y}}{2} \right], \end{aligned} \quad (12)$$

$$\begin{aligned} \int \mathcal{D} b_1^N \left(\frac{ib_2}{b_1} \right)^n \sin \mu z &= i^n e^{-\frac{\mu^2 w}{2}} \cosh^N(\mu w) \tanh^n(\mu w) \\ &\times \left[\frac{(-1)^n e^{i\mu y} - e^{-i\mu y}}{2i} \right], \end{aligned} \quad (13)$$

where n and μ are positive integers. We finally obtain

$$\begin{aligned} \langle 0|e^{-T^{\text{SD}}} J_x e^{T^{\text{SD}}} |0\rangle &= N e^{-2w} \cosh^N(2w) (1 + \tanh 2w) \\ &\times [2\alpha\beta \cos 2y + (\alpha^2 - \beta^2) \sin 2y]. \end{aligned} \quad (14)$$

The derivation of other terms in the CCSD energy is similar and the results are summarized in Appendix A 1. For the singles and doubles equations, instead of acting on $e^{-T} H e^T |0\rangle$ from the left with $\langle 0|$, one applies $\langle 1| = \langle 0|f_1$ and $\langle 12| = \langle 0|f_1 f_2$, respectively. Appendixes A 2 and A 3 summarize the terms used in the CCSD equations.

III. LOCAL MINIMUM AS ENVELOPE OF AVOIDED CROSSINGS

A. Model: Cubic potential in transverse field and antiferromagnetic interactions

As our first example, consider the Hamiltonian

$$H_{\text{cubic}} = -\frac{s\lambda}{N^2} (J_z)^3 + \frac{s(1-\lambda)}{N} (J_x)^2 - (1-s)J_x, \quad (15)$$

where the parameters $s, \lambda \in [0, 1]$ control the relative strengths among the three operators. This model was proposed in the context of quantum annealing [63], where one seeks to optimize the cubic objective function $(J_z)^3$ via careful adjustments of quantum fluctuations in the form of the transverse field J_x and antiferromagnetic interactions $(J_x)^2$. In the absence of the antiferromagnetic term, quantum annealing is highly inefficient due to a first-order phase transition. Antiferromagnetic fluctuations can, however, soften the transition to a second-order one, leading to a quantum speedup.

We have two reasons for studying this model. First, it is simple, exhibiting a single local minimum on the classical energy landscape. The second motivation is partly related to the first and concerns the identity and eventual fate of a local minimum in the process of annealing. The computational bottleneck of quantum annealing lies near the Landau-Zener crossing between the ground and first excited states. In the

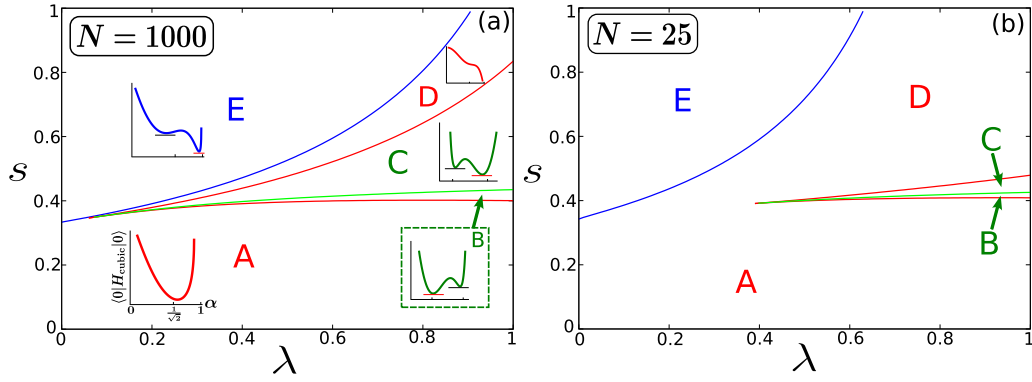


FIG. 1. Phase diagram of the cubic model H_{cubic} showing its classical energy landscape [Eq. (16)] in the s - λ plane. (a) $N = 1000$. (b) $N = 25$. The plane can be divided into five regions, labeled A to E. At finite N , one can go from region A to D without crossing a boundary, as seen from (b). In (a), a schematic of the energy landscape within a region is shown next to that region's label.

mean-field picture, these two states are embodied by the global and local minima, respectively. While this correspondence holds true near the avoided crossing, when away from the crossing, whether the local minimum still remains as the first excited state, becomes other eigenstates, or if the mean-field description breaks down altogether, is not very clear. In this respect, the simple energy landscape of this model allows us to follow the sole local minimum closely and study this issue without complications from other minima. As we shall show, at least for this model, the local minimum eventually evolves into a very high-energy eigenstate, implying bad results for quantum annealing if the system gets trapped by the minimum at the avoided crossing bottleneck.

B. Classical energy landscape and phase diagram

Due to permutation symmetry among all spins in H_{cubic} , the Hartree-Fock wave function takes the simpler form $|0\rangle = \binom{\alpha}{\beta}^N$, and one has

$$\begin{aligned} \langle 0 | H_{\text{cubic}} | 0 \rangle = & -s\lambda(N-1)(1-2N^{-1})(2\alpha^2-1)^3 \\ & -2N(1-s)\alpha\sqrt{1-\alpha^2} \\ & +4s(1-\lambda)(N-1)\alpha^2(1-\alpha^2) \\ & -s\lambda(3-2N^{-1})(2\alpha^2-1) + s(1-\lambda). \end{aligned} \quad (16)$$

One can summarize the overall behavior of the system in the form of a phase diagram in s - λ parameter space. Figure 1(a) shows the case for $N = 1000$. The phase space consists of five regions, labeled A to E. A schematic of the classical energy landscape within a region is shown next to that region's label. Boundaries between regions are obtained numerically. The energy landscape has one minimum in regions A and D, and two minima in B, C, and E. Our interest will be in the three latter regions, where the energy surface exhibits a local minimum. When going from region B to C, the system undergoes a first-order phase transition. As will be discussed below, only the local minimum in regions B and C exhibits quantum-classical correspondence, while the one in region E seems to be an unphysical minimum.

Figure 1(a) is representative of the phase diagram for general N . As N decreases, the most salient change is that region

C becomes smaller, as seen in Fig. 1(b) for the case of $N = 25$. When N is finite, regions A and D are not separated by a boundary. This is seen clearly in Fig. 1(b) where at small N the effect is more pronounced. As N increases, region D becomes smaller, with regions C and E merging in the thermodynamic limit. This narrowing of region D is, however, quite slow with respect to N as we were still able to observe the region numerically at $N = 40\,000$.

C. Ground-state energy

1. Hartree-Fock approximation

The Hamiltonian H_{cubic} commutes with the total angular momentum operator $J_x^2 + J_y^2 + J_z^2$, so the ground-state energy $E_0(H_{\text{cubic}})$ can be obtained numerically by diagonalizing H_{cubic} in the sector with total angular momentum $N/2$. The Hartree-Fock energy $E_0^{\text{HF}}(H_{\text{cubic}})$ is evaluated at the global minimum of Eq. (16). Figure 2(a) shows the difference between $E_0(H_{\text{cubic}})$ and $E_0^{\text{HF}}(H_{\text{cubic}})$ when $N = 1000$. To accentuate small differences, the fractional error $\frac{|E_0^{\text{HF}} - E_0|}{|E_0|}$ is plotted on logarithmic scale in the vertical axis. Each curve shows the error as a function of s at constant λ , representing a vertical slice through the phase diagram [cf. Fig. 1(a)]. The three curves convey an overall picture of the system's behavior. Generally speaking, although $E_0^{\text{HF}}(H_{\text{cubic}})$ approximates $E_0(H_{\text{cubic}})$ quite accurately when $s \lesssim 0.4$, the error is significant when $s \gtrsim 0.4$.

2. Coupled-cluster singles-doubles (CCSD) approximation

We now improve upon Hartree-Fock energy via CCSD approximation. Details are given in Appendixes A and B. Here we simply outline the procedure.

The CCSD excitation operator T^{SD} is given by Eq. (7). The singles equation is obtained by substituting Eqs. (A5), (A7), and (A9) into $\langle 1 | e^{-T^{\text{SD}}} H_{\text{cubic}} e^{T^{\text{SD}}} | 0 \rangle = 0$, and the doubles equation by substituting Eqs. (A10), (A12), and (A14) into $\langle 2 | e^{-T^{\text{SD}}} H_{\text{cubic}} e^{T^{\text{SD}}} | 0 \rangle = 0$. The equations are solved numerically to obtain the CCSD parameters y and w in Eq. (7), which are then substituted into $\langle 0 | e^{-T^{\text{SD}}} H_{\text{cubic}} e^{T^{\text{SD}}} | 0 \rangle$ via Eqs. (14), (A2), and (A4), yielding the CCSD energy $E_0^{\text{CC}}(H_{\text{cubic}})$. Figure 2(b) shows the fractional error between $E_0(H_{\text{cubic}})$ and

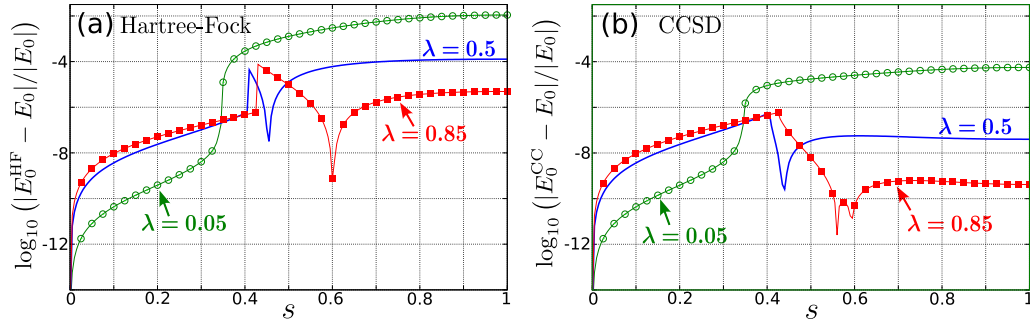


FIG. 2. Comparing the ground-state energy of the cubic model $E_0(H_{\text{cubic}})$ with (a) Hartree-Fock energy $E_0^{\text{HF}}(H_{\text{cubic}})$ and (b) CCSD energy $E_0^{\text{CC}}(H_{\text{cubic}})$, for $N = 1000$. Each curve shows the logarithm of the fractional error as a function of s at constant λ . It is seen that $E_0^{\text{CC}}(H_{\text{cubic}})$ gives an accurate approximation of $E_0(H_{\text{cubic}})$ when N is large.

$E_0^{\text{CC}}(H_{\text{cubic}})$. It is seen that CCSD leads to significant improvement in accuracy in the region $s \gtrsim 0.4$. This close agreement between $E_0(H_{\text{cubic}})$ and $E_0^{\text{CC}}(H_{\text{cubic}})$ improves even further as N increases. To summarize, when N is large CCSD energy is accurate enough to enable one to correlate it with an energy eigenvalue.

D. Local minimum in regions B and C

We now discuss the local minimum, here focusing on the one in regions B and C. Its CCSD energy, denoted as $E_{\text{local}}^{\text{CC}}(H_{\text{cubic}})$, is calculated in the same way as $E_0^{\text{CC}}(H_{\text{cubic}})$, with the Hartree-Fock wave function $|0\rangle$ evaluated at the local minimum of Eq. (16). Figure 3(b) shows $E_{\text{local}}^{\text{CC}}(H_{\text{cubic}})$ as a function of s ($\lambda = 0.5$, $N = 1000$). To track $E_{\text{local}}^{\text{CC}}(H_{\text{cubic}})$ as it evolves amidst the energy eigenvalues, one needs to look at the entire energy spectrum. Figure 3(a) shows the spectrum of H_{cubic} in the sector with total angular momentum $N/2$. We have plotted alternate levels using the same color to help the reader distinguish between individual eigenvalues. Each curve in Fig. 3(a) shows an energy level $E_n(H_{\text{cubic}})$ ($n = 0, \dots, N$) as a function of s . One discerns a densely colored band (green) spanning across the diagonal, which is a region where many energy levels undergo avoided crossings. Notice that the curve of $E_{\text{local}}^{\text{CC}}(H_{\text{cubic}})$ coincides with this band, which can be seen by comparing the two panels visually.

Figure 4 zooms in on the region where the CCSD energy coincides with the band. To facilitate visual inspection, the curve of $E_{\text{local}}^{\text{CC}}(H_{\text{cubic}})$ is superimposed on the full spectrum $E_n(H_{\text{cubic}})$, with the Hartree-Fock energy $E_{\text{local}}^{\text{HF}}(H_{\text{cubic}})$ subtracted from both energies. Figure 4(a) shows a closeup view of a narrow range of energy around the horizontal axis. One sees that an energy level sometimes exhibits a “z”-shaped kink in its curve, which is due to a succession of two avoided crossings with neighboring levels. Interestingly, these kinks chain together to form an envelope of avoided crossings, and several of these are seen in Fig. 4(a). The lowest one lies along the horizontal axis, which incidentally is also the Hartree-Fock energy. After CCSD correction, we see that the energy of the local minimum (blue circles) agrees almost exactly with the lowest envelope. Panels (i) to (iii) zoom in on three locations, indicated in Fig. 4(a), for closer inspection.

Hence, there appears to be a quantum-classical correspondence between the local minimum and the energy spectrum. Usually, one associates a classical energy state with a single energy level, as in the case of the ground state. Here, the local minimum is associated instead with an envelope of avoided crossings formed by concatenation of consecutive energy levels. This quantum-classical correspondence between the envelope and the local minimum improves when λ is closer to unity (constant N), and also as N increases. Nevertheless,

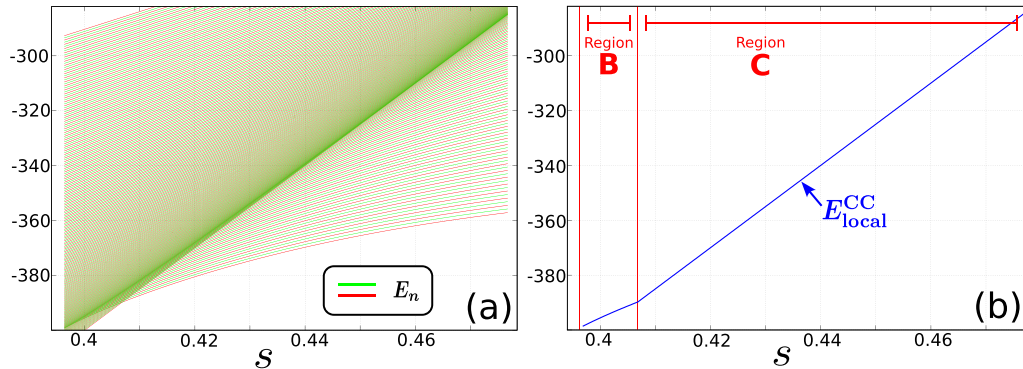


FIG. 3. Correspondence between quantum spectrum and classical energy of local minimum for the cubic model H_{cubic} ($\lambda = 0.5$, $N = 1000$). (a) The full energy spectrum as a function of s (sector of H_{cubic} with total angular momentum $N/2$). Alternate energy levels are plotted with the same color. The densely colored band spanning across the diagonal is a region with many avoided crossings among energy levels. (b) The CCSD energy of the local minimum $E_{\text{local}}^{\text{CC}}(H_{\text{cubic}})$ in the same range of s . The boundaries of regions B and C [cf. Fig. 1(a)] are also shown. Comparing the two panels, one sees that the curve (blue) in (b) coincides with the band (dense green) in (a).

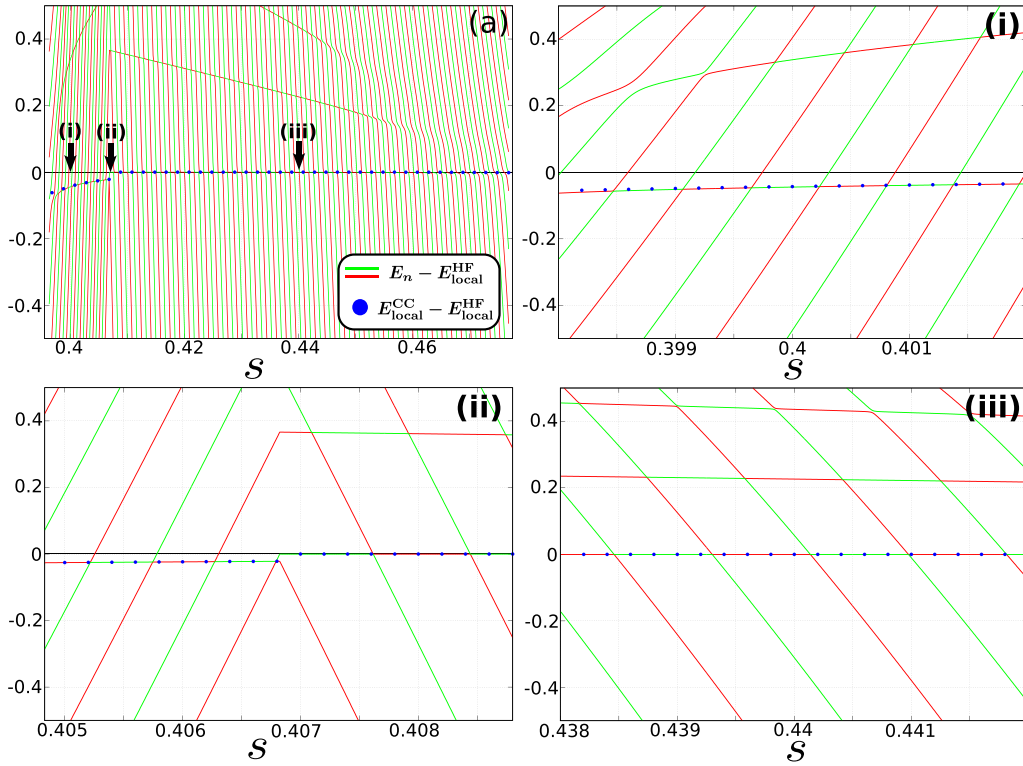


FIG. 4. Closeup view of Fig. 3, with the curve of $E_{\text{local}}^{\text{CC}}(H_{\text{cubic}})$ of Fig. 3(b) superimposed on the full spectrum of Fig. 3(a). The vertical axes here have been adjusted by subtracting the Hartree-Fock energy of the local minimum $E_{\text{local}}^{\text{HF}}(H_{\text{cubic}})$ from $E_{\text{local}}^{\text{CC}}$ and all the energy levels of the spectrum. The legend shown in (a) applies to all panels. (a) Closeup view of the horizontal axis (i.e., around the Hartree-Fock energy). (i) Closeup view of the region around $s = 0.4$, indicated in (a). (ii) Around $s = 0.407$, where the first-order phase transition occurs. (iii) Around $s = 0.44$. Overall, one sees that the CCSD energy of the local minimum coincides with the lowest envelope.

the correspondence is already apparent at smaller N . Figure 5 shows the CCSD energy superimposed on the energy spectrum at a smaller system size ($N = 75$, $\lambda = 0.65$). Again, one

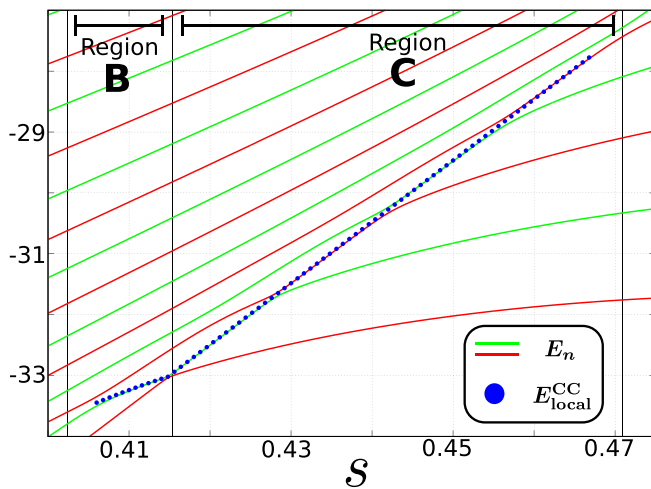


FIG. 5. Correspondence between the envelope of avoided crossings and the CCSD energy of local minimum $E_{\text{local}}^{\text{CC}}(H_{\text{cubic}})$ when the system size is small ($N = 75$, $\lambda = 0.65$). The figure is organized similar to Fig. 3, this time with $E_{\text{local}}^{\text{CC}}$ superimposed on the spectrum. The quantum-classical correspondence is observable even at this smaller system size.

sees that the CCSD energy coincides with the envelope of avoided crossings.

E. Wave functions along the envelope of avoided crossings

Let us examine the classical and quantum wave functions along the envelope. The energy eigenfunctions $|E_n(H_{\text{cubic}})\rangle$ are obtained from diagonalization and we represent them using the eigenfunctions of the J_z operator $|m_z\rangle$. The Hartree-Fock wave function of the local minimum $|E_{\text{local}}^{\text{HF}}(H_{\text{cubic}})\rangle$ is also represented using the same basis. Details on $|m_z\rangle$ and the calculation of $\langle m_z | E_{\text{local}}^{\text{HF}} \rangle$ are given in Appendix C.

To evince the correspondence between the wave functions, we define \tilde{n} as the level label such that the energy difference $|E_{\text{local}}^{\text{HF}}(H_{\text{cubic}}) - E_{\tilde{n}}(H_{\text{cubic}})|$ (fixed s and λ) is the smallest among all the energy eigenvalues; in other words, the eigenvalue closest to $E_{\text{local}}^{\text{HF}}$ is $E_{\tilde{n}}$. Figure 6 compares the probability densities $|\langle m_z | E_{\text{local}}^{\text{HF}} \rangle|^2$ (black circles) and $|\langle m_z | E_{\tilde{n}} \rangle|^2$ (red solid) at three locations of the envelope in Fig. 4(a); specifically, panels (i) to (iii) show for $s = 0.4$, 0.406 , and 0.44 , respectively. The densities of the two neighboring energy levels $|\langle m_z | E_{\tilde{n} \pm 1} \rangle|^2$ (blue dashed, green square) are also shown, for comparison. One sees that there is close correspondence between the classical state at the local minimum and the nearest energy eigenstate [64].

A more comprehensive picture can be attained by monitoring the overlap between the wave functions. Figure 7(a) shows the level label \tilde{n} along the envelope in Fig. 4(a), and Fig. 4(b)

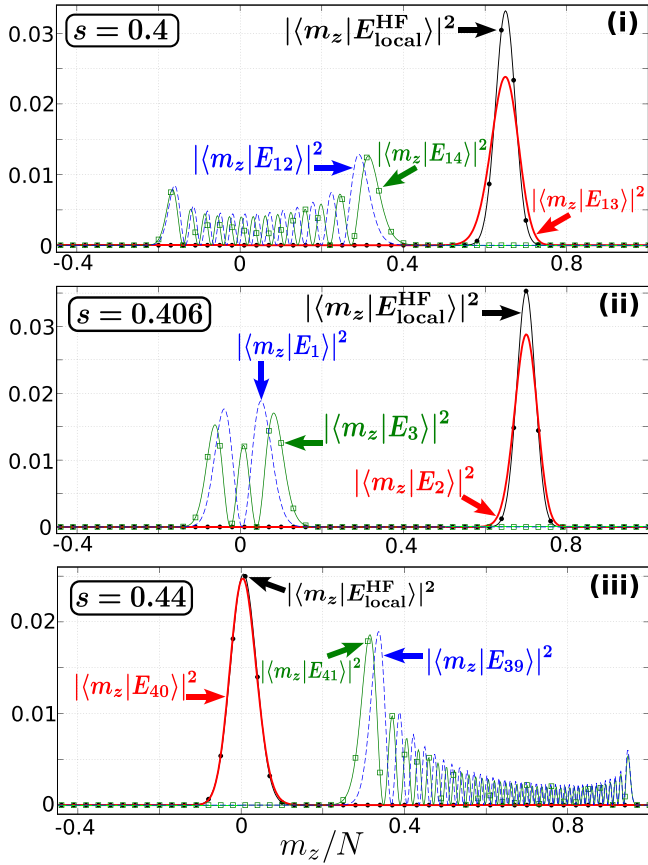


FIG. 6. Wave functions at three values of s along the envelope shown in Fig. 4(a). (i) $s = 0.4$. (ii) $s = 0.406$. (iii) $s = 0.44$. In each panel, the probability densities of the Hartree-Fock wave function $\langle m_z | E_{\text{local}}^{\text{HF}} \rangle$ (circle) and the three nearest energy eigenfunctions $\langle m_z | E_{\tilde{n}} \rangle$ (solid) and $\langle m_z | E_{\tilde{n} \pm 1} \rangle$ (dashed and square) are plotted. One sees that the classical $\langle m_z | E_{\text{local}}^{\text{HF}} \rangle$ has a quantum counterpart in $\langle m_z | E_{\tilde{n}} \rangle$.

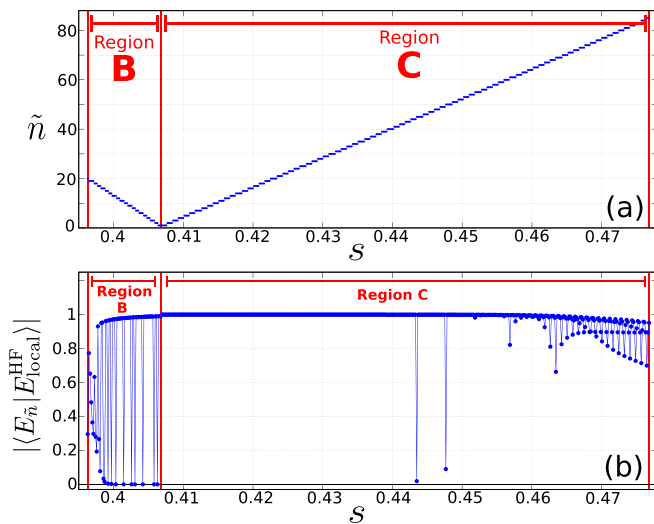


FIG. 7. (a) Level label \tilde{n} along the envelope in Fig. 4(a). (b) Overlap $\langle E_{\tilde{n}} | E_{\text{local}}^{\text{HF}} \rangle$ between the Hartree-Fock wave function at the local minimum and the nearest energy eigenfunction, along the envelope. Lines connecting data points (circles) are to guide the eye only. The overlap is close to unity along the entire envelope.

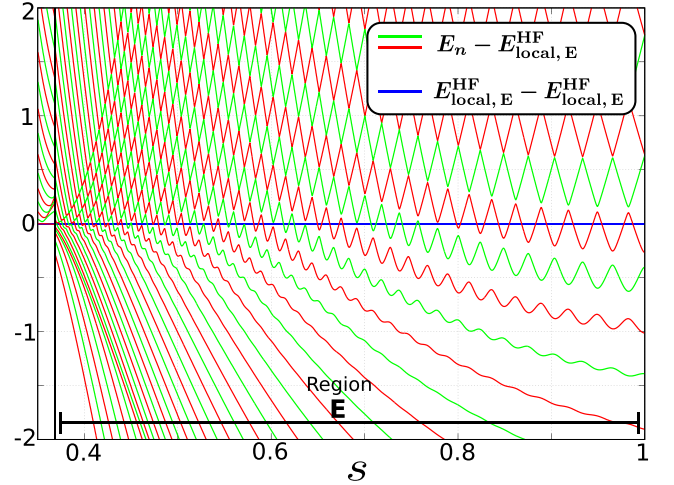


FIG. 8. No quantum-classical correspondence for the local minimum in region E ($N = 100$, $\lambda = 0.1$). The Hartree-Fock energy of the local minimum, denoted $E_{\text{local}, E}^{\text{HF}}(H_{\text{cubic}})$ (blue), is superimposed on the energy spectrum (red and green). The vertical axis has been shifted by $E_{\text{local}, E}^{\text{HF}}$, as in Fig. 4. Visually, there appears to be no correspondence between the classical and quantum energies.

shows the overlap $\langle E_{\tilde{n}} | E_{\text{local}}^{\text{HF}} \rangle$. We see that the overlap is very close to unity along the entire envelope. (Sudden deteriorations at isolated points are due to avoided crossings, where $E_{\tilde{n}}$ and $E_{\tilde{n}-1}$ are almost degenerate.)

We close this section with a short comment. In this model, we were able to evince the quantum-classical correspondence partly because the Hamiltonian commutes with the total angular momentum. This had allowed us to focus on the energy spectrum of one sector (with $N + 1$ levels) instead of the entire spectrum (with 2^N levels), greatly simplifying our visual inspection of the classical and quantum energies. In general, however, when the Hamiltonian does not exhibit any symmetry, such correspondences, if present, will be difficult to discover due to the much higher density of levels in the spectrum.

F. Unphysical local minimum in region E

One might ask whether all the local minima on the classical energy landscape has correspondences in the quantum spectrum. Figure 8 compares the Hartree-Fock energy of the local minimum in region E, denoted $E_{\text{local}, E}^{\text{HF}}(H_{\text{cubic}})$, with the energy spectrum (for $N = 100$, $\lambda = 0.1$). The figure is organized similar to Fig. 4, with the Hartree-Fock energy subtracted along the vertical axis. One sees that the energy of the local minimum (horizontal axis, blue) cuts across many levels, and visually there does not appear to be any correspondence between the classical and quantum energies. We tried solving the CCSD equations at this local minimum, but were unable to obtain any solutions (perhaps another indication that the minimum is not physically meaningful). In analogy to Fig. 7(b), we examined the overlap of the Hartree-Fock wave function with the nearest energy eigenfunction, and found that the overlap is small (between 0 and 0.6). Hence, it is also possible that a local minimum is unphysical.

IV. QUANTUM-CLASSICAL CORRESPONDENCE IN A FRUSTRATED SYSTEM

A. Hopfield model in transverse field

The cubic model is not frustrated and its energy surface is relatively simple. Let us now consider a frustrated one, the Hopfield model in transverse field [65–67]

$$H_{\text{Hop}} = -\frac{1}{2N} \sum_{\mu=1}^p [J_z(\xi^\mu)]^2 - \Gamma J_x, \quad (17)$$

where $J_z(\xi^\mu)$ is defined by Eq. (4), and Γ is the strength of the transverse field. The original Hopfield model, without the transverse field, was proposed in a classical context within the field of associative memory [68]. ξ^μ is an N -dimensional binary vector with components $+1$ or -1 . A total of p such vectors are embedded as memory patterns, which are to be retrieved from the temporal dynamics of the system. The original model was subsequently generalized to Eq. (17) by various authors [65–67]. Recently, this model is receiving renewed attention in diverse fields such as quantum machine learning [69], image recognition [70], and quantum computing [71].

Apart from its wide range of applications, we are motivated to study this model mainly because it is very flexible in the sense that the complexity of its energy landscape is tunable via the embedded patterns ξ^μ . For finite loading where the ratio $\frac{p}{N}$ is nonzero in the thermodynamic limit, the Hopfield model crosses over into the Sherrington-Kirkpatrick model and exhibits spin-glass behavior. However, as the dimension of the Hilbert space is very large, it is not feasible to diagonalize the Hamiltonian matrix numerically in this regime. On the other hand, in the low loading regime where $p \ll N$ at finite N , the energy landscape still retains some vestige of ruggedness where local minima are located near to the patterns ξ^μ in configuration space. It is in this regime that we shall study the model since we have some control over the energy surface via our choice of patterns, and also because we can study a small system size whose Hamiltonian matrix is amenable to exact numerical diagonalization. The case of uncorrelated patterns (each $\xi_i^\mu = +1$ or -1 with equal probability) in the low loading regime has been studied analytically using mean-field approximation by Nishimori and Nonomura [67]. Using our Hartree-Fock framework, discussed below, we were able to verify their predictions on the structure of the free-energy landscape. On the other hand, the case of correlated patterns is harder to treat analytically and has received lesser attention by comparison. We shall therefore focus on such patterns in this work.

It is not feasible to perform an exhaustive study of all possible pattern combinations. In the following we shall focus instead on just one set of correlated patterns [72]. Table I shows the correlations among the patterns as measured by the inner product $\xi^\mu \cdot \xi^\nu = N^{-1} \sum_{i=1}^N \xi_i^\mu \xi_i^\nu$. It is seen that there is significant correlation among the embedded patterns. This instantiation has parameters $N = 16$ and $p = 4$. We are limited to these small values because it is computationally expensive both to obtain the energy eigenvalues and eigenstates, and to perform a thorough sampling of the energy landscape.

TABLE I. Correlations among the embedded patterns ξ^μ (cf. [72]) and Hartree-Fock solutions $\tilde{\alpha}_n$ (at $\Gamma = 0$) for the instance of H_{Hop} being studied ($N = 16, p = 4$). Correlation between \mathbf{a} and \mathbf{b} is measured by $\mathbf{a} \cdot \mathbf{b} = N^{-1} \sum_{i=1}^N a_i b_i$. The last column lists the energy, Eq. (21), at \mathbf{a} with $\Gamma = 0$.

$\mathbf{a} \cdot \mathbf{b}$					
\mathbf{a}/\mathbf{b}	ξ^1	ξ^2	ξ^3	ξ^4	Energy
$\xi^1, \tilde{\alpha}_5$	1	0	0	0	-8
$\xi^2, \tilde{\alpha}_4$	0	1	-0.25	0	-8.5
$\xi^3, \tilde{\alpha}_2$	0	-0.25	1	0.25	-9
$\xi^4, \tilde{\alpha}_3$	0	0	0.25	1	-8.5
$\tilde{\alpha}_1$	0.25	0.5	-0.75	-0.5	-9
$\tilde{\alpha}_6$	0.5	-0.5	0	0.5	-6

B. Hartree-Fock approximation

As ξ_i^μ is binary, there are 2^p possible combinations of the tuple $(\xi_1^1, \dots, \xi_1^p)$, and each spin label i belongs to one of the combinations. Let a combination be labeled γ . The N spins can then be divided into 2^p groups where all the spins in each group belong to the same combination. The Hamiltonian (17) can be rewritten as

$$H_{\text{Hop}} = -\frac{1}{2N} \sum_{\mu=1}^p \left[\sum_{\gamma=1}^{2^p} \xi_\gamma^\mu J_z^\gamma \right]^2 - \Gamma \sum_{\gamma=1}^{2^p} J_x^\gamma, \quad (18)$$

where ξ_γ^μ denotes the component of the μ th pattern in the tuple γ , and modifying Eq. (4) slightly we define

$$J_\alpha^\gamma = \sum_{i_\gamma=1}^{N_\gamma} \sigma_{i_\gamma}^\alpha, \quad (19)$$

where i_γ labels a spin in the group of γ , and N_γ is the total number of spins in the group. Equation (18) simply makes the grouping of the spins manifest, and is equivalent to Eq. (17). The point is that one can work with a Hartree-Fock wave function with reduced dimensionality

$$|0\rangle = \prod_{\gamma=1}^{2^p} \left[\prod_{i_\gamma=1}^{N_\gamma} \begin{pmatrix} \alpha_{i_\gamma} \\ \beta_{i_\gamma} \end{pmatrix} \right] = \prod_{\gamma=1}^{2^p} \begin{pmatrix} \alpha_\gamma \\ \beta_\gamma \end{pmatrix}^{N_\gamma} \quad (20)$$

instead of Eq. (1). The second equality emphasizes that all the spins within a group exhibit permutation symmetry. The classical energy surface is then

$$\begin{aligned} \langle 0 | H_{\text{Hop}} | 0 \rangle = & -\frac{1}{2N} \sum_{\mu=1}^p \left[\sum_{\gamma} N_\gamma \xi_\gamma^\mu (2\alpha_\gamma^2 - 1) \right]^2 \\ & + \frac{p}{2N} \sum_{\gamma} N_\gamma (2\alpha_\gamma^2 - 1)^2 \\ & - \frac{p}{2} - 2\Gamma \sum_{\gamma} N_\gamma \alpha_\gamma \sqrt{1 - \alpha_\gamma^2}. \end{aligned} \quad (21)$$

Equation (21) is valid for arbitrary patterns. Substituting the instantiation of patterns mentioned above leads to a seven-dimensional function for $\langle 0 | H_{\text{Hop}} | 0 \rangle$.

C. Visualization of high-dimensional energy landscape

In this section, we examine the classical energy (21) in detail.

1. $\Gamma = 0$

Let us first consider the case of $\Gamma = 0$ (i.e., no transverse field). We obtained all the energy minima numerically. An initial condition is randomly chosen, and its energy minimized using zero-temperature Metropolis algorithm. This process is repeated, each time starting from a different initial condition, until all minima are found. Six solutions, and their spin-flipped counterparts, were obtained. Each solution is then converted back to an N -dimensional spin-labeled vector $\vec{\alpha}$ where the component of the i_γ th spin $(\vec{\alpha})_{i_\gamma}$ is related to its Hartree-Fock solution α_γ by

$$(\vec{\alpha})_{i_\gamma} = 2\alpha_\gamma^2 - 1. \quad (22)$$

Four of the six solutions coincide with the embedded patterns. The correlations of the remaining two solutions, denoted $\vec{\alpha}_1$ and $\vec{\alpha}_6$, are shown in Table I. These so-called spurious states correspond to incorrect recall of the memorized patterns. The last column of Table I gives the Hartree-Fock energies of the six solutions. It is seen that the spurious state $\vec{\alpha}_1$ is one of the ground states.

The vectors $\vec{\alpha}_n$ are high dimensional. Let us introduce a plotting system to visualize them. An N -dimensional vector \mathbf{a} can be projected onto the polar coordinates (r, θ) , where r is the normalized Euclidean distance of \mathbf{a} from the origin vector ω ,

$$r^2 = \frac{1}{4N} \sum_{i=1}^N (a_i - \omega_i)^2, \quad (23)$$

and θ is the angle between \mathbf{a} and the pole vector \mathbf{p} ,

$$\theta = \cos^{-1} \left[\frac{\mathbf{a} \cdot \mathbf{p}}{(\mathbf{a} \cdot \mathbf{a})(\mathbf{p} \cdot \mathbf{p})} \right] \quad (24)$$

with the inner product $\mathbf{a} \cdot \mathbf{p}$ defined in the caption of Table I. Figure 9 shows the plot of the polar coordinates of all the energy minima $\vec{\alpha}_n$, where r and θ are plotted as the radial and angular displacements, respectively. We have chosen ω and \mathbf{p} such that all the $\vec{\alpha}_n$ have distinct coordinates [73]. The spin-flipped solutions (denoted $-\vec{\alpha}_n$) and the embedded patterns (green open circles) are also shown. The global minima are indicated by solid circles (blue), while local minima are plotted in red.

This method of plotting provides a way to visualize high-dimensional energy landscapes. As a first example, consider the energy of the original Hopfield model, which is defined on the vertices of an N -dimensional cube. Let us denote \mathcal{E}_{Hop} as the energy of H_{Hop} evaluated at the 2^N classical spin configurations [i.e., Eq. (17) with $\Gamma = 0$]. The definition of \mathcal{E}_{Hop} differs slightly from Eq. (21) in that the latter is a continuous function and takes into account spin permutation symmetry. Figure 10 shows the energy landscape of \mathcal{E}_{Hop} based on the plotting system used for displaying the energy minima. The polar coordinates of a spin configuration are calculated in the same way as for the minima, and the \mathcal{E}_{Hop} of the configuration is indicated by color. If more than one configuration is mapped

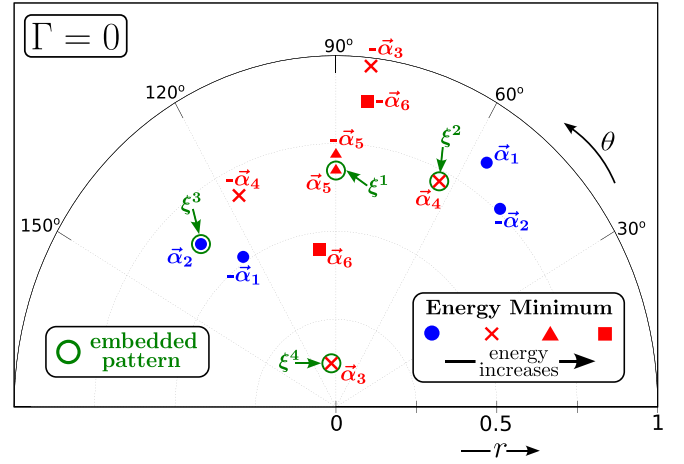


FIG. 9. Polar plot showing the relative positions of all the energy minima of Eq. (21) when $\Gamma = 0$, instantiated by the patterns [72]. The coordinates (r, θ) of a Hartree-Fock solution $\vec{\alpha}_n$ are plotted as the radial and angular displacements, with ω and \mathbf{p} given by [73]. Spin-flipped solutions are denoted $-\vec{\alpha}_n$. Global minima are plotted with solid circles (blue), local minima in red, and the embedded patterns with open circles (green).

onto the same polar coordinates, the lowest \mathcal{E}_{Hop} is adopted. The energy minima shown in Fig. 9 are also plotted here, using the same symbols (green). In this heat map, high-energy regions are indicated by warm colors. With this system of plotting, one can gain some intuition into the topography of the energy function \mathcal{E}_{Hop} . For instance, the relative depth among the minima, the energy barriers separating them, as well as possible transition pathways, can all be discerned from the plot.

This method of plotting can also be applied to the classical energy (21). In this case, the configuration space is

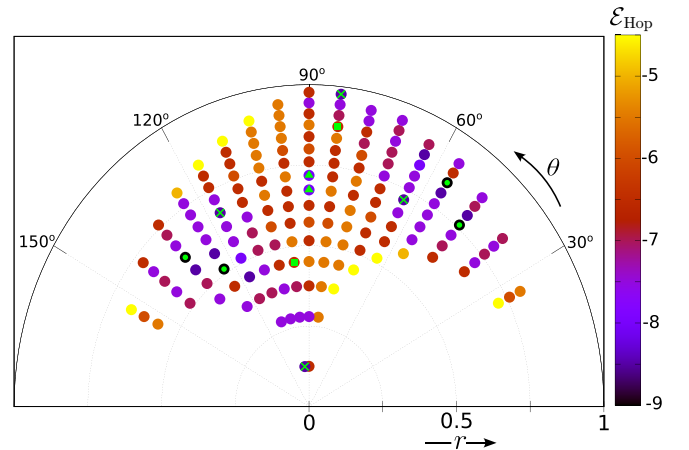


FIG. 10. Visualizing the landscape of the energy \mathcal{E}_{Hop} . The energy minima in Fig. 9 are reproduced using the same symbols (green). Each solid circle represents the polar coordinates of a point in configuration space, with its energy \mathcal{E}_{Hop} indicated by color. Higher-energy regions are indicated by warmer colors. The topography of the high-dimensional energy surface can be discerned from this polar plot.

continuous, so we set up a discrete rectangular grid in the r - θ plane. A randomly sampled point in configuration space is first projected onto polar coordinates, and then assigned to the appropriate bin in the grid. If the energy of the sampled point is lower than the energy already registered in the bin, replace the previous energy with the new one. This sampling process is repeated until there are no further updates in all the bins. Figure 11(a) shows the energy landscape of $\langle 0|H_{\text{Hop}}|0\rangle$ when $\Gamma = 0$, obtained via uniform sampling of configuration space 10^{11} times. For presentation purposes, the polar coordinates are plotted in Cartesian format. Energy minima (green) are also indicated, as in Fig. 10. The heat map allows us to visualize the ruggedness of the energy landscape, which is usually difficult for high-dimensional surfaces. For instance, we can discern topographical features such as corridors connecting energy basins (narrow blue channels), as well as the shape and size of each basin (black patches).

2. $\Gamma > 0$

Let us now turn on the transverse field. We tracked the evolution of all the energy minima numerically as Γ is increased. Denote the Hartree-Fock energy of the minimum $\pm\tilde{\alpha}_n$ as $E_{\pm n}^{\text{HF}}(H_{\text{Hop}})$. Figure 12(a) shows how the energy of each minimum varies with Γ . Note that the free energy $F = -(N/2)(1 + \Gamma^2)$ [67] has been subtracted from the curves. One sees that the local minima disappear from the energy surface at different Γ . At $\Gamma = 0.55$, for example, only the local minima $\pm\tilde{\alpha}_5$ are remaining on the surface.

The procedure for plotting Fig. 11(a) can also be applied to $\Gamma > 0$ to visualize the evolution of the energy surface with Γ . The landscapes at $\Gamma = 0.27$ and 0.55 , indicated in Fig. 12(a) by vertical lines, are shown in Figs. 11(b) and 11(c), respectively. In addition to the vanishing of the local minima, one can also see the smoothening of the energy surface with increase in Γ .

To round up this section on classical energy landscape, let us look at how the positions of the minima change with Γ . Figure 12(b) shows the evolution of the polar coordinates of the minima as Γ increases. The paramagnetic state, located at the geometric center of configuration space, is indicated by a semicircle. It is seen that the global minima $\pm\tilde{\alpha}_1$ trace out rather complicated paths when evolving towards the paramagnetic state.

D. Localization of excited eigenstates in the energy basins of local minima

We now bring in the quantum aspects of the model. The energy eigenvalues $E_n(H_{\text{Hop}})$ and the corresponding eigenvectors are obtained using the Lanczos algorithm [74]. As the ground state has been discussed in many previous works, in the following we shall focus on the local minima.

Figure 13(a) shows the energy levels around the fourfold-degenerate Hartree-Fock energy $E_{\pm 3,4}^{\text{HF}}$ (blue circles). The levels E_4 to E_7 (highlighted in red) are closest to it. There is some disagreement between the classical and quantum energies, originating from the smallness of the system size. Nevertheless, convincing evidences of quantum-classical correspondence can still be discerned by examining the wave

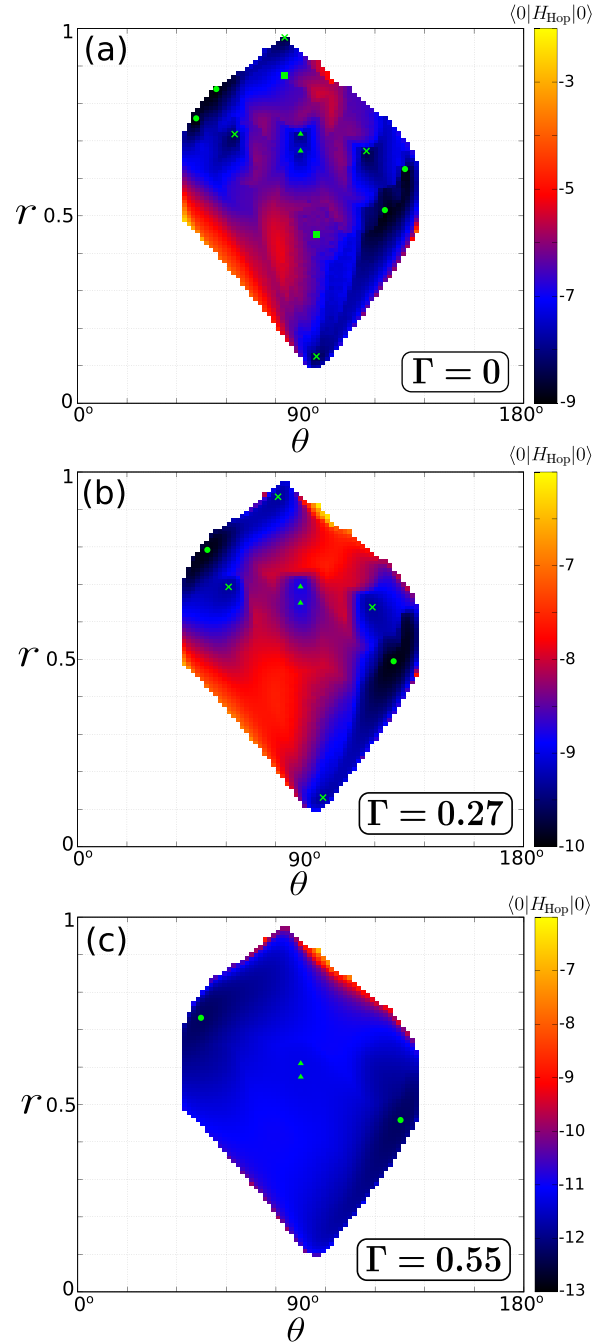


FIG. 11. Visualizing the landscape of the classical energy $\langle 0|H_{\text{Hop}}|0\rangle$ at different Γ . Polar coordinates are plotted in Cartesian format, with θ for abscissa and r for ordinate. Energy minima present at each Γ are indicated with the same symbols (green) used in Fig. 9. (a) At $\Gamma = 0$. (b) At $\Gamma = 0.27$. (c) At $\Gamma = 0.55$. One discerns the smoothening of the landscape and the vanishing of the minima with increase in Γ .

functions. Table II shows the overlaps between the four eigenfunctions $|E_4\rangle$ to $|E_7\rangle$ and the four Hartree-Fock wave functions $|E_{\pm 3,4}^{\text{HF}}\rangle$, taken at $\Gamma = 0.1$ and 0.32 [vertical lines in Fig. 13(a)]. As the overlap between a $|E_n\rangle$ and each of the $|E_m^{\text{HF}}\rangle$ differ by only a sign, for compactness the square of the overlap $|\langle E_m^{\text{HF}}|E_n\rangle|^2$ is shown. At $\Gamma = 0.1$, the projections of, say $|E_4\rangle$, onto the four Hartree-Fock states account

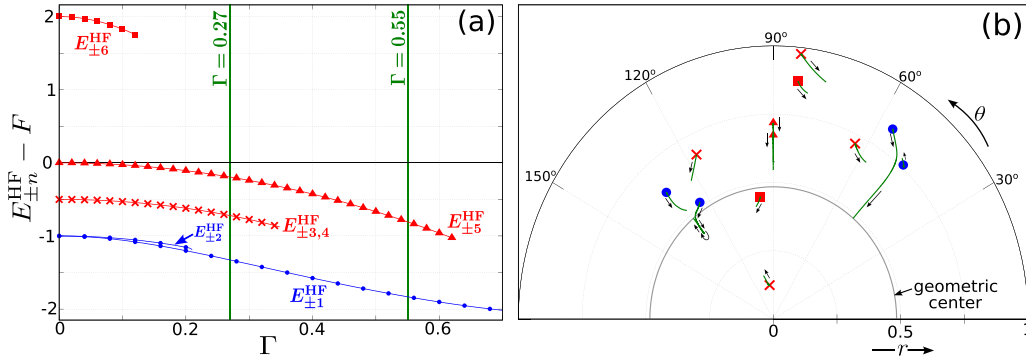


FIG. 12. Evolutions of the energies and positions of the minima of $\langle 0|H_{\text{Hop}}|0\rangle$ with Γ . (a) Hartree-Fock energy $E_n^{\text{HF}}(H_{\text{Hop}})$ of the minimum $\vec{\alpha}_n$ as a function of Γ , adjusted by the free energy F . At $\Gamma = 0.27$, $\pm\vec{\alpha}_{2,6}$ have vanished from the energy surface; at $\Gamma = 0.55$, only $\pm\vec{\alpha}_{1,5}$ are left. (b) Polar coordinates of the minima. Starting from $\Gamma = 0$ (cf. Fig. 9), each minimum evolves along a trajectory where the accompanying arrows indicate the direction of increasing Γ . The paramagnetic state, located at the geometric center of configuration space, is also indicated.

for $4 \times 23 = 92\%$ of its probability mass, meaning that the eigenfunction is localized mainly in the four local minima $\pm\vec{\alpha}_{3,4}$. This behavior is exhibited by the other three eigenfunctions as well. The high degree of overlap between the quantum and classical states persists, dropping only slightly, until $\Gamma = 0.32$, just before the minima vanish from the energy surface.

The next minima $\pm\vec{\alpha}_5$ present some additional features. Figure 13(b) shows the energy levels around the twofold degenerate $E_{\pm 5}^{\text{HF}}$ (blue circles). In this case, two groups of levels are involved: E_{14}, E_{15} (red) and E_{16}, E_{17} (green). It is seen that there is an avoided crossing between $E_{14,15}$ and $E_{16,17}$ at $\Gamma \approx 0.26$. Before the crossing, localization is manifested by the eigenfunctions $|E_{16}\rangle$ and $|E_{17}\rangle$. For instance, at $\Gamma = 0.25$, projecting $|E_{16}\rangle$ onto the two Hartree-Fock states gives $|\langle E_5^{\text{HF}}|E_{16}\rangle|^2 + |\langle E_{-5}^{\text{HF}}|E_{16}\rangle|^2 \approx 2 \times 0.48 = 0.96$. After the crossing, the localizations are inherited by $|E_{14}\rangle$ and $|E_{15}\rangle$. For example, at $\Gamma = 0.28$ projection of $|E_{14}\rangle$ gives $|\langle E_5^{\text{HF}}|E_{14}\rangle|^2 + |\langle E_{-5}^{\text{HF}}|E_{14}\rangle|^2 \approx 2 \times 0.44 = 0.88$. The localizations persist until $\Gamma = 0.4$, where the projections drop to 0.66 for $|E_{14}\rangle$ and 0.57 for $|E_{15}\rangle$, after which the overlaps between the quantum and classical states decay very rapidly.

One can visualize the eigenstates' localizations using the method of plotting the energy landscape presented earlier. We performed the Lanczos algorithm in the σ_i^z representation, and each energy eigenfunction is returned as a superposition of 2^N classical spin configurations. Each basis vector (a spin configuration) is first projected onto the r - θ plane and assigned to

the appropriate grid bin. Then, instead of updating the energy, we accumulate the probability (i.e., amplitude squared) of the basis vector onto the histogram at that bin. As an example, Fig. 14 shows the localization of the eigenstate $|E_{14}\rangle$ around the minima $\pm\vec{\alpha}_5$ at $\Gamma = 0.28$ [cf. Fig. 13(b), just after the avoided crossing]. The heat map shows the classical energy landscape where the energy basin of $\pm\vec{\alpha}_5$ is the blue oval at the center. The histogram of $|E_{14}\rangle$ is shown as symbols (green) superimposed on the energy landscape. For clarity, only the 12 bins with the highest cumulative probability are shown. The circle symbols each carry a probability of ≈ 0.25 . The probabilities at each of the cross symbols are actually not equal, but on average each carries a probability of ≈ 0.03 . It is seen that more than 80% of the probability mass of $|E_{14}\rangle$ is localized around the energy basin of the minima $\pm\vec{\alpha}_5$.

It is instructive to compare our polar plot (Fig. 14) to the Fock space diagram introduced by Mukherjee *et al.* for visualizing many-body localization delocalization [39]. The authors examined how high-energy eigenvectors of the Sherrington-Kirkpatrick model exhibit localization delocalization as the strength of the transverse field changes. In their work, each of the 2^N basis configurations is given a label $i \in [0, 2^N - 1]$ and mapped onto coordinates $i \rightarrow (i_A, i_B)$; the amplitudes of an eigenvector are then plotted on the two-dimensional i_A - i_B plane in the form of a heat map. Their diagram reveals the MBLD transition in a visual way. However, in this system of plotting the label i assigned to a basis configuration is somewhat arbitrary, and the physical significance of the coordinates (i_A, i_B) is not very clear. On the other hand, in our polar plot the coordinates (r, θ) are always referenced to the classical energy surface, so our diagram is more informative. For instance, changes in the energy landscape with the parameter Γ are reflected in the polar plot, so the mechanism underlying the shifts in positions of the eigenfunction amplitudes with Γ becomes evident. If one were to visualize this with the Fock space diagram, only the shifts of the amplitudes in i_A - i_B space would be visible, with no insights on localization.

E. Unphysical local minima at $\pm\vec{\alpha}_6$

We now turn our attention to the final local minima $\pm\vec{\alpha}_6$. These have the highest Hartree-Fock energy among all the

TABLE II. Squares of the overlap $|\langle E_{\pm 3,4}^{\text{HF}}|E_n\rangle|^2$ between the Hartree-Fock wave functions at the local minima $\pm\vec{\alpha}_{3,4}$ and the eigenfunctions $|E_4\rangle$ to $|E_7\rangle$ of the Hopfield model, evaluated at $\Gamma = 0.1$ and 0.32 [cf. Fig. 13(a)]. The overlaps $\langle E_{\pm 3,4}^{\text{HF}}|E_n\rangle$ of each $|E_m^{\text{HF}}\rangle$ with a $|E_n\rangle$ are identical apart from a sign.

Γ	$ \langle E_{\pm 3,4}^{\text{HF}} E_n\rangle ^2$			
	E_4	E_5	E_6	E_7
0.1	0.23	0.23	0.23	0.23
0.32	0.23	0.23	0.21	0.21

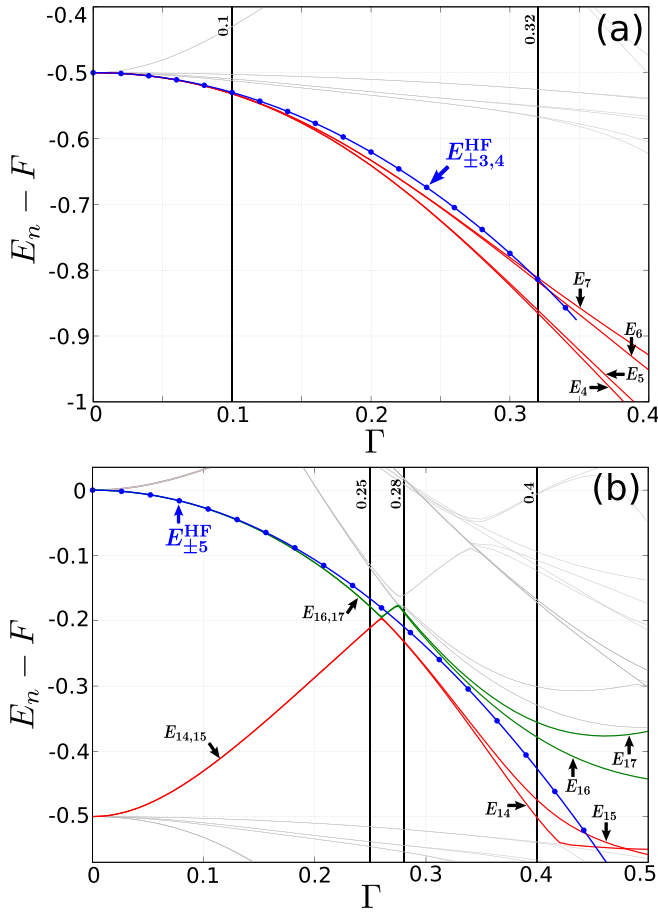


FIG. 13. Energy eigenvalues $E_n(H_{\text{Hop}})$ in the vicinity of (a) $E_{\pm 3,4}^{\text{HF}}$ and (b) $E_{\pm 5}^{\text{HF}}$ [cf. Fig. 12(a)]. The levels E_n are plotted with solid lines. Curves of Hartree-Fock energy are adorned with circles (blue). All energies are shifted by the free energy F . Identities of the levels closest to the Hartree-Fock energy are labeled and colored (red, green), while irrelevant levels are plotted in gray. Vertical lines indicate the Γ values where the energy eigenfunctions are examined.

minima, and from the landscape diagram Fig. 11(a) one can also see that their energy basins are relatively shallow. Unlike for the other minima, we were unable to establish quantum-classical correspondence for $\pm \tilde{\alpha}_6$. Figure 15 shows the energy levels around the twofold degenerate $E_{\pm 6}^{\text{HF}}$ (blue circles). There is an avoided crossing at $\Gamma = 0.08$ ($E_n - F \approx 1.83$). We first focus our discussion on the Γ regime before the crossing.

TABLE III. Squared overlaps $|\langle E_{\pm 6}^{\text{HF}} | E_n \rangle|^2$ of the Hopfield model for the minima $\pm \tilde{\alpha}_6$, evaluated at $\Gamma = 0.07$. Only six eigenfunctions, $|E_{420}\rangle$ to $|E_{423}\rangle$, $|E_{434}\rangle$, and $|E_{435}\rangle$, exhibit appreciable overlaps with the Hartree-Fock states $|E_{\pm 6}^{\text{HF}}\rangle$. As in Table II, $\langle E_6^{\text{HF}} | E_n \rangle$ and $\langle E_{-6}^{\text{HF}} | E_n \rangle$ differ only by a sign. The small overlaps suggest that $\pm \tilde{\alpha}_6$ have no correspondence with physical states.

$ \langle E_{\pm 6}^{\text{HF}} E_n \rangle ^2$		
$E_{420,421}$	$E_{422,423}$	$E_{434,435}$
0.11	0.18	0.12

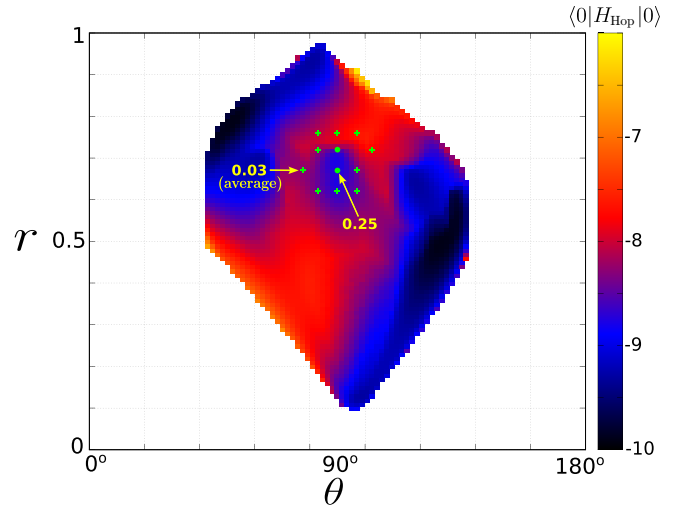


FIG. 14. Localization of the eigenstate $|E_{14}\rangle$ around the energy basins of the minima $\pm \tilde{\alpha}_5$ at $\Gamma = 0.28$. The heat map shows the energy landscape of $\langle 0 | H_{\text{Hop}} | 0 \rangle$. The eigenfunction $|E_{14}\rangle$ is projected onto the r - θ plane, and the circle and cross symbols (green) indicate the locations with the highest cumulative probability. Arrows indicate the probability carried by each symbol. It is seen that more than 80% of the probability mass of $|E_{14}\rangle$ is localized around $\pm \tilde{\alpha}_5$.

We scanned through the overlaps between $|E_{\pm 6}^{\text{HF}}\rangle$ and all the eigenstates $|E_n\rangle$ and found that $\langle E_{\pm 6}^{\text{HF}} | E_n \rangle$ is appreciable only for six of the eigenstates. The energy levels of these six eigenstates are labeled in Fig. 15 (highlighted in red). Generally speaking, even for these six states the overlaps are quite low. For instance, the squared overlaps $|\langle E_{\pm 6}^{\text{HF}} | E_n \rangle|^2$ at $\Gamma = 0.07$ (vertical line in Fig. 15) are listed in Table III. It is seen that for, say $|E_{420}\rangle$, only $2 \times 11 \approx 22\%$ of its probability mass is accounted for by $|E_{\pm 6}^{\text{HF}}\rangle$. One can also ascertain this visually

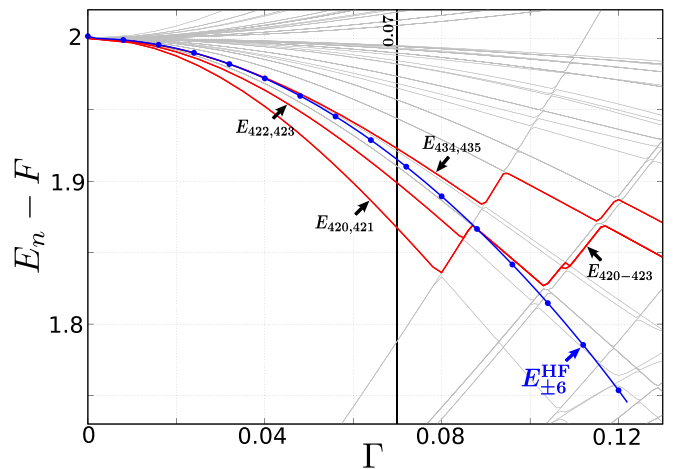


FIG. 15. Energy eigenvalues E_n of the Hopfield model in the vicinity of the highest Hartree-Fock energy $E_{\pm 6}^{\text{HF}}$. The figure is organized similar to Fig. 13. Discussion in the text focuses on the region before the first avoided crossing at $\Gamma \approx 0.08$. The labeled energy levels (red) are those whose eigenfunctions exhibit the largest overlaps with $|E_{\pm 6}^{\text{HF}}\rangle$ before the crossing. The wave-function overlaps at $\Gamma = 0.07$ (vertical line) are given in Table III.

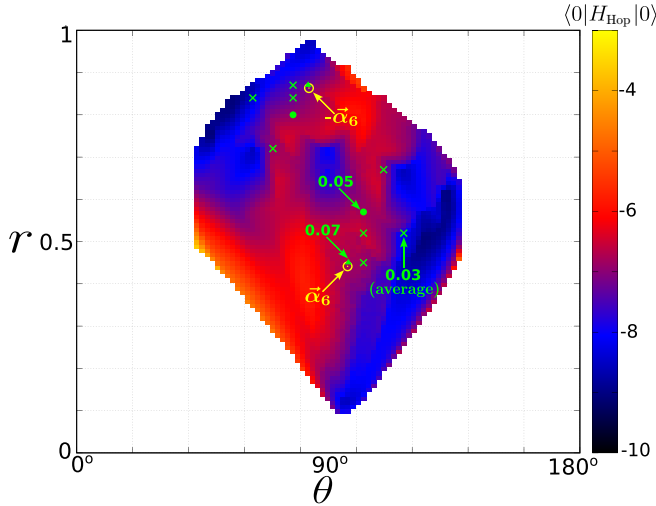


FIG. 16. Projection of the eigenstate $|E_{420}\rangle$ at $\Gamma = 0.07$ onto the r - θ plane. The figure is organized similar to Fig. 14. The heat map shows the energy landscape at $\Gamma = 0.07$, with the minima $\pm\tilde{\alpha}_6$ indicated by empty circles (yellow). The other symbols (green) represent the locations where $|E_{420}\rangle$ has the highest cumulative probability. We see that only about 20% of the probability mass of the eigenfunction is close to $\pm\tilde{\alpha}_6$.

by projecting an eigenstate onto the r - θ plane and comparing it with the energy landscape, as we have done for $|E_{14}\rangle$ earlier. Figure 16 shows the probability histogram of $|E_{420}\rangle$ at $\Gamma = 0.07$ superimposed on the classical energy landscape. For clarity of presentation, only the 12 largest bins, comprising approximately 50% of the total probability mass, are plotted (green symbols). The local minima $\pm\tilde{\alpha}_6$ are indicated by empty circles (yellow). One sees that only about 20% of the probability mass of $|E_{420}\rangle$ is located close to $\pm\tilde{\alpha}_6$. Overall, it seems that the minima $\pm\tilde{\alpha}_6$ cannot be associated with any of the energy eigenstates.

After the first avoided crossing at $\Gamma = 0.08$, the relationship between $\pm\tilde{\alpha}_6$ and the energy levels becomes rather complex because of the subsequent crossings. We tracked the overlaps in the manner discussed above until $\Gamma = 0.12$, and found that the behavior, nevertheless, remains similar. Hence, like the cubic model, for the Hopfield model one can also encounter unphysical local minima.

F. Incorporation of coupled-cluster effects

Hitherto, our discussions have centered around the Hartree-Fock energy. We tried incorporating coupled-cluster excitations into the classical energy, but did not obtain improvement in accuracy for the particular realization of Hopfield model being studied here. For singles excitations, the coupled-cluster energy and equations can be derived by applying the results of Appendix A to individual J_α^γ operators in Eq. (18). At the global minima $\pm\tilde{\alpha}_1$, we found that the singles energy is higher than the Hartree-Fock energy $E_{\pm 1}^{\text{HF}}$, and is numerically less accurate than the latter. Furthermore, as we increase Γ beyond ≈ 0.1 , the basin of attraction of the singles solution diminishes while spurious solutions appear, making it difficult to identify and attain the correct solution. At the local minima, the accuracy issue is even more acute as the singles

energies that we managed to obtain are very far from both the Hartree-Fock and quantum energies. We also implemented a limited version of doubles excitations where the two excited spins both lie within the same group γ , and so the CCSD energy and equations can again be derived using the results of Appendix A. The effects of doubles excitations are, however, very small and do not affect our above conclusions. Despite these results, we think that the discouraging performance of CCSD in our case study is largely due to the smallness of our system size ($N = 16$). As our detailed analysis of the ferromagnetic model in Appendix B shows, CCSD becomes very accurate when the system size is large. In that regime, numerical diagonalization of the Hamiltonian is no longer feasible, so our formulas in Appendix A may come in useful in numerical studies of frustrated quantum spin systems.

V. SUMMARY AND DISCUSSIONS

In this paper, we performed a detailed numerical investigation on the relationship between the energy eigenstates and the local minima on the energy landscape of quantum spin systems. We adopted an empirical approach, working with specific models, so the results here might not be generally applicable to every system. Nonetheless, we think that the illustrations here can shed some insights on the quantum-classical correspondence between the two quantities.

We studied two models, and found that the local minima on the classical energy landscape can be interpreted as excited eigenstates in the energy spectrum. The first model is a nonfrustrated one exhibiting a single local minimum. Here, it was found that the minimum corresponds to an envelope of avoided crossings, which is a secondary structure on the energy spectrum. The second model is a frustrated one exhibiting multiple local minima. In this case, we found energy eigenfunctions which are localized in the energy basins of the minima. Apart from these affirmative cases, however, we also found instances of unphysical local minima, so one needs to exercise some caution when applying these observations to other systems.

One possible extension of this work might be in the classification or labeling of the energy levels of frustrated systems. In nonfrustrated models such as Eqs. (15) and (B1), the total angular momentum is conserved, so its quantum number can be used to classify the energy levels of the system into different sectors. On the other hand, for frustrated systems such as Eq. (17), it is not *a priori* clear what the conserved quantity, if it exists, should be. For such systems, one might consider assigning labels to levels based on the energy basin (or basins) which they are associated with. It would be interesting to see how the excitations in a basin can be generated within the equation-of-motion framework [50,75], and if the correspondence reported here continues to be valid. These labels could then serve as generalized “quantum numbers” for frustrated systems.

In our studies of the Hopfield model, we noticed some features of its energy spectrum that might be indicative of a path to quantum chaos. In Figs. 13(b) and 15, there is a regime of weak transverse field (small Γ) where the spectrum is regular in the sense that there are no collisions among the energy levels. The appearance of the first avoided crossing then initiates

a cascade of complex level collisions in subsequent larger Γ values. This transition from regular to “level-collision” phase can be quantitatively characterized by various measures based on level statistics [29,30]. Curiously, the disappearance of local minima from the energy surface [cf. Fig. 12(a)] occurs in the vicinity of this onset of chaos. It might be interesting to examine whether there is any relationship between the two in our future studies.

As mentioned in the Introduction, one of the purposes of this work is to study the feasibility of the coupled-cluster method as a numerical technique for quantum spin systems. Perhaps the most important observation we made is that the existence of solutions (to the coupled-cluster equations) depends on the system size and also on parameters within the model. Generally speaking, the method tends to break down near second-order phase transitions and at small system sizes. Hence, the coupled-cluster expansion is not uniformly convergent and does not provide improvement upon the Hartree-Fock approximation unconditionally. On the other hand, for pure systems at large system sizes, we found the method to be quite reliable and accurate. It remains to assess its performance for disordered systems at large system size in our future studies.

In this work, we implemented CCSD using the random field approach. Higher-order excitations can be treated similarly. For instance, quadruples and triples excitations can be written as $X^4 = (X^2)^2$ and $4X^3 = (X + X^2)^2 - (X - X^2)^2$, after which linearization can be achieved by repeated applications of the Hubbard-Stratonovich transform. Cross terms can be treated similarly: $4XY = (X + Y)^2 - (X - Y)^2$. It might be worth mentioning that the Fourier transform of the Airy function

$$e^{\frac{i}{3}(2\pi X)^3} = \int_{-\infty}^{\infty} \text{Ai}(k) e^{-2\pi i k X} dk \quad (25)$$

allows us to linearize a cubic term X^3 at the price of just a single random field variable k . This additional economy might help simplify the derivation of the coupled-cluster energy and equations.

We briefly comment on our usage of Eqs. (4) to (6). The formulas in Appendix A are derived by setting the vector \mathbf{a} in $J_\alpha(\mathbf{a})$ to unity, which did not utilize the full generality of the three relations. For more complicated models such as the Sherrington-Kirkpatrick model, the formulas in the Appendix are no longer applicable, and one should employ the more general framework when dealing with such systems.

Lastly, let us touch upon the accuracy of Hartree-Fock approximation. In the course of our study, we found that Hartree-Fock approximation is sometimes quite inaccurate as a leading approximation, especially at large system sizes. On the other hand, note that in the quantum TAP approach [28], inclusion of the Onsager correction is necessary. This correction removes the effects of self-response in the internal field, and is important when dealing with random systems. Curiously, such a correction term does not arise in the traditional Hartree-Fock framework, and this might account for some of its inadequacies as a mean-field approximation. It would be interesting to see if terms analogous to the Onsager correction can be accommodated within the Hartree-Fock framework so as to yield a more accurate leading approximation.

ACKNOWLEDGMENTS

This work is partly funded by a project commissioned by the New Energy and Industrial Technology Development Organization (NEDO) of Japan. We also thank the anonymous referees for their valuable comments.

APPENDIX A: SUMMARY OF FORMULAS FOR COUPLED-CLUSTER THEORY

This Appendix is a continuation of the derivation given in Sec. II. In the following, to simplify notations, we omit the superscript from T^{SD} , and define $e_n \equiv e^{-nw}$, $c_n \equiv \cosh(nw)$, $t_n \equiv \tanh(nw)$, $\tilde{c}_n \equiv \cos(ny)$, and $\tilde{s}_n \equiv \sin(ny)$.

1. For CCSD energy $\langle 0 | e^{-T} H e^T | 0 \rangle$

The CCSD energies in this paper can be obtained by combining appropriate terms from Eq. (14) and the following list of expressions.

$$\langle 0 | e^{-T} J_z e^T | 0 \rangle = N e_2 c_2^N (1 + t_2) [2\alpha\beta\tilde{s}_2 - (\alpha^2 - \beta^2)\tilde{c}_2], \quad (A1)$$

$$\langle 0 | e^{-T} J_x^2 e^T | 0 \rangle = N + \frac{N(N-1)}{2} \{ 1 + e_8 c_4^N (1 + t_4)^2 [4\alpha\beta(\alpha^2 - \beta^2)\tilde{s}_4 - [(\alpha^2 - \beta^2)^2 - 4\alpha^2\beta^2]\tilde{c}_4] \} \quad (A2)$$

$$\langle 0 | e^{-T} J_z^2 e^T | 0 \rangle = N + \frac{N(N-1)}{2} \{ 1 - e_8 c_4^N (1 + t_4)^2 [4\alpha\beta(\alpha^2 - \beta^2)\tilde{s}_4 - [(\alpha^2 - \beta^2)^2 - 4\alpha^2\beta^2]\tilde{c}_4] \}, \quad (A3)$$

$$\begin{aligned} \langle 0 | e^{-T} J_z^3 e^T | 0 \rangle = & -\frac{N(N-1)(N-2)}{4} e_{18} c_6^N (1 + t_6)^3 \{ 2\alpha\beta(3 - 16\alpha^2\beta^2)\tilde{s}_6 + (\alpha^2 - \beta^2)(16\alpha^2\beta^2 - 1)\tilde{c}_6 \} \\ & - \frac{3N}{4} e_2 c_2^N (1 + t_2) [N(N+1) - (N-1)(N-2)t_2^2] [2\alpha\beta\tilde{s}_2 - (\alpha^2 - \beta^2)\tilde{c}_2] \\ & - \frac{N}{2} e_{18} c_6^N (1 - t_6) [2\alpha\beta\tilde{s}_6 + (\alpha^2 - \beta^2)\tilde{c}_6]. \end{aligned} \quad (A4)$$

2. For singles equation $\langle 1 | e^{-T} H e^T | 0 \rangle = 0$

The singles equations in this paper can be obtained by combining appropriate terms from the following list of expressions.

$$\langle 1 | e^{-T} J_x e^T | 0 \rangle = e_2 c_2^N [1 + N t_2 + (N-1)t_2^2] [2\alpha\beta\tilde{s}_2 - (\alpha^2 - \beta^2)\tilde{c}_2], \quad (A5)$$

$$\langle 1|e^{-T} J_z e^T |0\rangle = e_2 c_2^N [1 + N t_2 + (N-1) t_2^2] [2\alpha\beta\tilde{c}_2 + (\alpha^2 - \beta^2)\tilde{s}_2], \quad (\text{A6})$$

$$\langle 1|e^{-T} J_x^2 e^T |0\rangle = (N-1)e_8 c_4^N (1+t_4)^2 \left(1 + \frac{N-2}{2} t_4\right) \{[4\alpha^2\beta^2 - (\alpha^2 - \beta^2)^2]\tilde{s}_4 - 4\alpha\beta(\alpha^2 - \beta^2)\tilde{c}_4\}, \quad (\text{A7})$$

$$\langle 1|e^{-T} J_z^2 e^T |0\rangle = -\langle 1|e^{-T} J_x^2 e^T |0\rangle, \quad (\text{A8})$$

$$\begin{aligned} \langle 1|e^{-T} J_z^3 e^T |0\rangle &= e_2 c_2^N (1+t_2) [2\alpha\beta\tilde{c}_2 + (\alpha^2 - \beta^2)\tilde{s}_2] \\ &\times \left\{ (3N-2)[1 + (N-1)t_2] + \frac{3(N-1)(N-2)}{4} (1-t_2^2)[1 + (N-3)t_2] \right\} \\ &+ \frac{(N-1)(N-2)}{4} e_{18} c_6^N [3 + (N-3)t_6] (1+t_6)^3 [2\alpha\beta(3 - 16\alpha^2\beta^2)\tilde{c}_6 + (\alpha^2 - \beta^2)(1 - 16\alpha^2\beta^2)\tilde{s}_6]. \end{aligned} \quad (\text{A9})$$

3. For doubles equation $\langle 12|e^{-T} H e^T |0\rangle = 0$

The doubles equations in this paper can be obtained by combining appropriate terms from the following list of expressions.

$$\langle 12|e^{-T} J_x e^T |0\rangle = -e_2 c_2^N t_2 [2 + N t_2 + (N-2)t_2^2] [2\alpha\beta\tilde{c}_2 + (\alpha^2 - \beta^2)\tilde{s}_2], \quad (\text{A10})$$

$$\langle 12|e^{-T} J_z e^T |0\rangle = e_2 c_2^N t_2 [2 + N t_2 + (N-2)t_2^2] [2\alpha\beta\tilde{s}_2 - (\alpha^2 - \beta^2)\tilde{c}_2], \quad (\text{A11})$$

$$\begin{aligned} \langle 12|e^{-T} J_x^2 e^T |0\rangle &= 1 + e_8 c_4^N (1+t_4)^2 \left\{ 1 + 2(N-2)t_4 + \frac{(N-2)(N-3)}{2} t_4^2 \right\} \\ &\times \{[(\alpha^2 - \beta^2)^2 - 4\alpha^2\beta^2]\tilde{c}_4 - 4\alpha\beta(\alpha^2 - \beta^2)\tilde{s}_4\}, \end{aligned} \quad (\text{A12})$$

$$\begin{aligned} \langle 12|e^{-T} J_z^2 e^T |0\rangle &= 1 - e_8 c_4^N (1+t_4)^2 \left\{ 1 + 2(N-2)t_4 + \frac{(N-2)(N-3)}{2} t_4^2 \right\} \\ &\times \{[(\alpha^2 - \beta^2)^2 - 4\alpha^2\beta^2]\tilde{c}_4 - 4\alpha\beta(\alpha^2 - \beta^2)\tilde{s}_4\}, \end{aligned} \quad (\text{A13})$$

$$\begin{aligned} \langle 12|e^{-T} J_z^3 e^T |0\rangle &= e_2 c_2^N [2\alpha\beta\tilde{s}_2 - (\alpha^2 - \beta^2)\tilde{c}_2] \left\{ (3N-2)t_2 [2 + N t_2 + (N-2)t_2^2] \right. \\ &\quad \left. - \frac{3(N-2)}{2} c_2^{-2} (1+t_2)[1 - (N-3)t_2 - \frac{(N-3)(N-4)}{2} t_2^2] \right\} \\ &+ \frac{3(N-2)}{2} e_{18} c_6^N (1+t_6)^3 \left\{ 1 + (N-3)t_6 + \frac{(N-3)(N-4)}{6} t_6^2 \right\} \\ &\times [2\alpha\beta(3 - 16\alpha^2\beta^2)\tilde{s}_6 + (\alpha^2 - \beta^2)(16\alpha^2\beta^2 - 1)\tilde{c}_6]. \end{aligned} \quad (\text{A14})$$

APPENDIX B: CCSD APPROXIMATION OF FERROMAGNETIC MODEL

In this Appendix, we illustrate the implementation of CCSD by applying it to the ferromagnetic model in transverse field

$$H_{\text{ferro}} = -(J/N)(J_z)^2 - \Gamma J_x, \quad (\text{B1})$$

where J and Γ are the strengths of the ferromagnetic coupling and the transverse field, respectively. This is perhaps the simplest fully connected quantum spin model possible. Nevertheless, even the ground-state energy is not analytically solvable when N is finite. In the thermodynamic limit $N \rightarrow \infty$, as Γ is lowered the ground state undergoes a second-order phase transition from a paramagnet to a ferromagnet at the critical point $\Gamma_c = 2J$. The ground-state energy of this

model under configuration interaction singles-doubles (CISD) approximation was studied previously in Ref. [7]. The results here therefore also offer some insights into how CCSD improves upon CISD.

1. Hartree-Fock approximation

The Hartree-Fock energy of H_{ferro} is obtained by minimizing

$$\langle 0|H_{\text{ferro}}|0\rangle = -J(N-1)(2\alpha^2 - 1)^2 - 2N\Gamma\alpha\sqrt{1 - \alpha^2} - J \quad (\text{B2})$$

with respect to α . The energy surface exhibits no local minimum, and the solution is $\alpha_0 = 1/\sqrt{2}$ when $\Gamma \geq 2J(1 - N^{-1})$

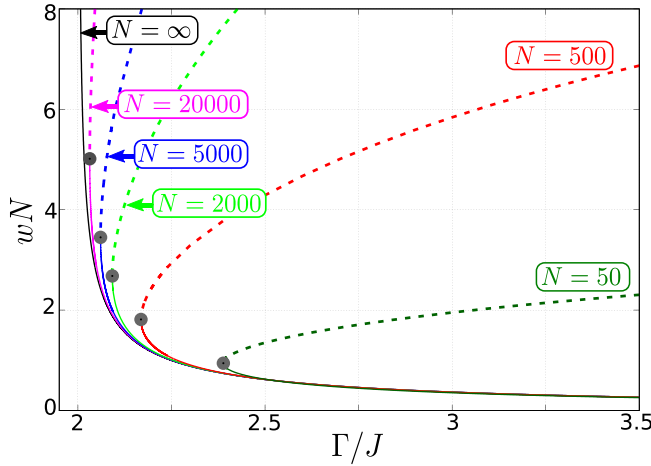


FIG. 17. Numerical solutions of w for the ferromagnetic model H_{ferro} in the paramagnetic regime ($\Gamma \geq 2J$), where the solution of y is zero. The results for several values of N are shown, and each curve has been rescaled by N . The solution has an upper (dashed) and a lower (solid) branch, and their meeting point is indicated by a solid circle. Only the lower branch is physically valid, and the lower branches of different N collapse together after rescaling. For finite N , w has no valid solution after the meeting point. The curve labeled $N = \infty$ (black) is the analytical solution in the thermodynamic limit, given by Eq. (B5).

(paramagnet), and

$$\alpha_{\pm} = \sqrt{\frac{1 \pm \sqrt{1 - \left(\frac{N}{N-1} \frac{\Gamma}{2J}\right)^2}}{2}} \quad (\text{B3})$$

when $\Gamma < 2J(1 - N^{-1})$ (ferromagnet), where α_+ and α_- are related by a spin flip. The Hartree-Fock energy is

$$E_0^{\text{HF}}(H_{\text{ferro}}) = \begin{cases} -N\Gamma - J & \text{when } \Gamma \geq 2J(1 - N^{-1}), \\ -N\left(\frac{N}{N-1} \frac{\Gamma^2}{4J} + J\right) & \text{when } \Gamma < 2J(1 - N^{-1}). \end{cases} \quad (\text{B4})$$

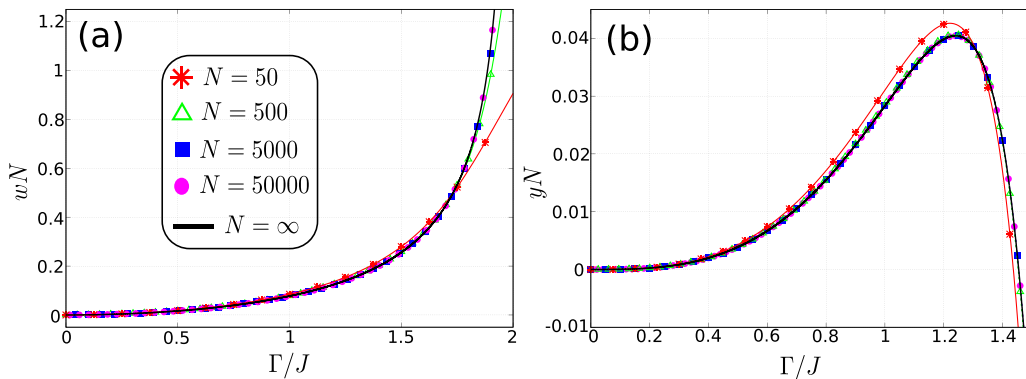


FIG. 18. Numerical solutions of (a) w and (b) y for the model H_{ferro} in the ferromagnetic regime ($\Gamma < 2J$). The results for several values of N are shown. Symbols have the same meaning in both panels. The vertical axes have been rescaled, to highlight that the solutions of different N collapse together upon rescaling. The curves labeled $N = \infty$ (black) are the analytical solutions in the thermodynamic limit, and are given by Eq. (B5) [for (a)] and Eq. (B6) [for (b)].

2. Solutions of CCSD equations

The singles equation is obtained by substituting Eqs. (A5) and (A8) into $\langle 1 | e^{-T^{\text{SD}}} H_{\text{ferro}} e^{T^{\text{SD}}} | 0 \rangle$, and the doubles equations (A10) and (A13) into $\langle 12 | e^{-T^{\text{SD}}} H_{\text{ferro}} e^{T^{\text{SD}}} | 0 \rangle$. The equations are solved numerically to obtain y and w . In the paramagnetic regime $\Gamma \geq 2J$, one has the solution $y = 0$, and Fig. 17 shows the solution of w for several values of N . The solution consists of an upper (dashed) and a lower (solid) branch, meeting at the point $(\Gamma_N, w_N N)$ indicated by a solid circle (gray). Only the lower branch is physically valid. The lower branches of different N collapse together upon rescaling (note the vertical axis). For finite N , there is no valid solution of w after the meeting point. Numerically, we found that Γ_N approaches the critical point Γ_c asymptotically as $\Gamma_N - \Gamma_c \sim 3.3 \times N^{-0.47}$, while $w_N \sim 0.32 \times N^{-0.73}$.

Figure 18 shows the solutions for y and w in the ferromagnetic regime $\Gamma < 2J$. Once again, the solutions of different N collapse together after rescaling.

3. CCSD energy

The CCSD energy $E_0^{\text{CC}}(H_{\text{ferro}})$ is obtained by inserting the solutions of y and w into Eqs. (14) and (A3), which are in turn substituted into $\langle 0 | e^{-T^{\text{SD}}} H_{\text{ferro}} e^{T^{\text{SD}}} | 0 \rangle$. We consider the difference between $E_0^{\text{CC}}(H_{\text{ferro}})$ and the exact ground-state energy $E_0(H_{\text{ferro}})$, obtained numerically via diagonalization [as done for Eq. (15)]. Figures 19(a) and 19(b) show the error $E_0^{\text{CC}}(H_{\text{ferro}}) - E_0(H_{\text{ferro}})$ in the paramagnetic and ferromagnetic regimes, respectively. The results for several values of N are shown. It is seen that the agreement between $E_0^{\text{CC}}(H_{\text{ferro}})$ and $E_0(H_{\text{ferro}})$ improves as N increases, with error occurring mainly around the critical point. To highlight the close agreement between the two energies, the insets show the errors replotted on logarithmic scale.

It is instructive to see how CCSD fare compared to Hartree-Fock approximation and CISD. For general aspects of configuration interaction expansion, the reader is referred to Refs. [49,50]. The CISD approximation of H_{ferro} was studied in Ref. [7]. Figure 20 shows $E_0^{\text{HF}}(H_{\text{ferro}})$, $E_0^{\text{CC}}(H_{\text{ferro}})$, and the CISD energy $E_0^{\text{CI}}(H_{\text{ferro}})$ as a function of Γ , with the exact energy $E_0(H_{\text{ferro}})$ subtracted from all three approximations.

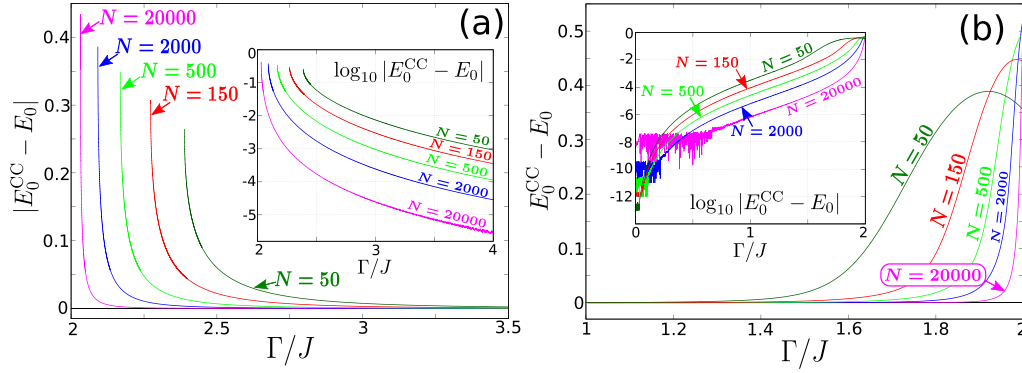


FIG. 19. Error between the CCSD energy $E_0^{\text{CC}}(H_{\text{ferro}})$ and the numerically exact ground-state energy $E_0(H_{\text{ferro}})$ of the model H_{ferro} , in the (a) paramagnetic and (b) ferromagnetic regimes. Results for several values of N are shown. One sees that the error decreases as N increases. Insets: The errors replotted on logarithmic scale.

Figures 20(a) and 20(b) show the results for $N = 20$ (small system size) and 500 (large), respectively. In general, CCSD shows evident improvement over CISD in the paramagnetic regime, both for small and large system sizes. In the ferromagnetic regime, however, the advantage of CCSD over CISD only manifests itself when N is large. This observation is in line with the fact that coupled-cluster theory accounts for extensivity better than configuration interaction expansion. Another notable difference between CISD and CCSD is that for the former the energy $E_0^{\text{CI}}(H_{\text{ferro}})$ always exists, whereas for the latter there is a small region around the critical point where $E_0^{\text{CC}}(H_{\text{ferro}})$ disappears. The reason for the vanishing of the CCSD energy is not immediately clear. One possible

explanation is that third- and higher-order effects begin to dominate the correlation energy around the transition point. In that case, it might be possible to recover the coupled-cluster energy by incorporating, say, three- and four-body excitations into the operator T .

4. Analytical solutions of w , y , and $E_0^{\text{CC}}(H_{\text{ferro}})$ in the limit $N \rightarrow \infty$

In the limit $N \rightarrow \infty$, it is possible to obtain analytical solutions of w and y . In the CCSD equations, make a change of variable $x = e^{2w}$ followed by $x = 1 + \delta$; expanding to second order in δ , one solves a quadratic equation in δ to obtain

$$w = \begin{cases} \frac{1}{2N} \left(\sqrt{\frac{\Gamma}{\Gamma - 2J}} - 1 \right) + O(N^{-2}) & \text{when } \Gamma \geq 2J, \\ \frac{1}{2N} \left(\sqrt{\frac{4J^2}{4J^2 - \Gamma^2}} - 1 \right) + O(N^{-2}) & \text{when } \Gamma < 2J. \end{cases} \quad (\text{B5})$$

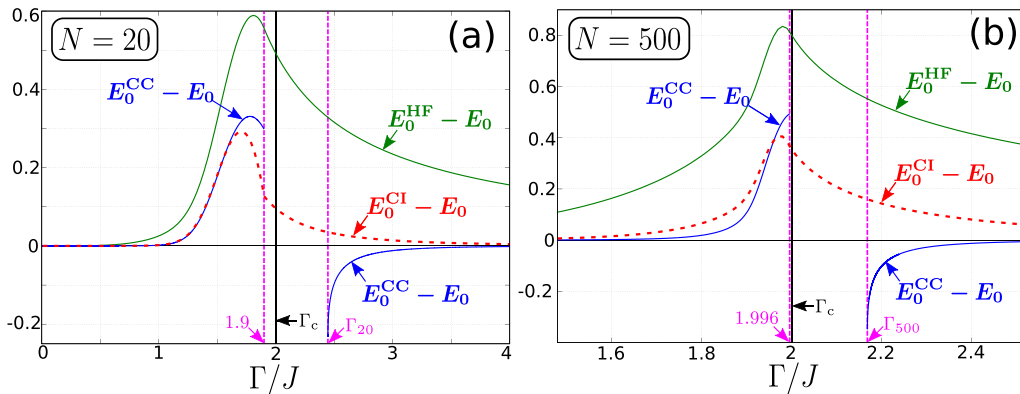


FIG. 20. Comparing the accuracy of the approximations $E_0^{\text{HF}}(H_{\text{ferro}})$, $E_0^{\text{CC}}(H_{\text{ferro}})$, and $E_0^{\text{CI}}(H_{\text{ferro}})$ for the model H_{ferro} . The exact energy $E_0(H_{\text{ferro}})$ has been subtracted from all three. The solid vertical line (black) indicates the critical point Γ_c . There is no solution for $E_0^{\text{CC}}(H_{\text{ferro}})$ between the two dashed vertical lines (magenta), where the left line marks the transition point of $E_0^{\text{HF}}(H_{\text{ferro}})$ [cf. Eq. (B4)] and the right one marks the vanishing of the solution of w [cf. Fig. 17]. (a) For $N = 20$. (b) For $N = 500$.

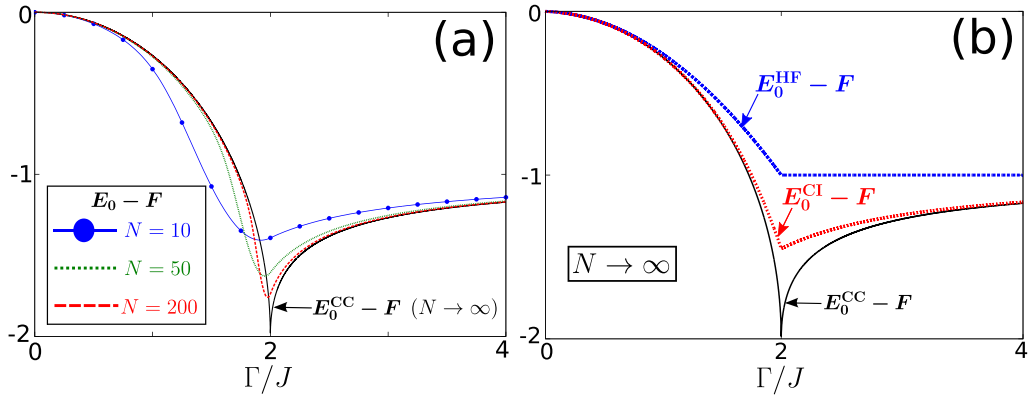


FIG. 21. (a) Convergence of the exact ground-state energy $E_0(H_{\text{ferro}})$ (colored) towards the thermodynamic CCSD energy $E_0^{\text{CC}}(H_{\text{ferro}})$ [Eq. (B7)] as N increases. The free energy F is defined in the text. (b) Comparison between the three energies $E_0^{\text{HF}}(H_{\text{ferro}})$, $E_0^{\text{CI}}(H_{\text{ferro}})$, and $E_0^{\text{CC}}(H_{\text{ferro}})$ in the limit $N \rightarrow \infty$.

and

$$y = \begin{cases} 0 & \text{when } \Gamma \geq 2J, \\ \frac{\Gamma}{4N} \left(\frac{\Gamma^2 - 16J^2}{(4J^2 - \Gamma^2)^{\frac{3}{2}}} + \frac{12J}{4J^2 - \Gamma^2} - \frac{1}{J} \right) + O(N^{-2}) & \text{when } \Gamma < 2J. \end{cases} \quad (\text{B6})$$

Equations (B5) and (B6) are plotted in Figs. 17 and 18 (labeled $N \rightarrow \infty$). It is seen that they agree quite well with the numerical results of large N .

Inserting the solutions Eqs. (B5) and (B6) into $E_0^{\text{CC}}(H_{\text{ferro}})$ and expanding in powers of N^{-1} , one obtains for the CCSD energy in the thermodynamic limit

$$E_0^{\text{CC}}(H_{\text{ferro}}) = \begin{cases} -N\Gamma + \sqrt{\Gamma(\Gamma - 2J)} - \Gamma + O(N^{-1}) & \text{when } \Gamma \geq 2J, \\ -N \left(\frac{4J^2 + \Gamma^2}{4J} \right) + \sqrt{4J^2 - \Gamma^2} - 2J + O(N^{-1}) & \text{when } \Gamma < 2J. \end{cases} \quad (\text{B7})$$

On the right side of Eq. (B7), the leading term proportional to N is also known as the free energy, which we denote as F . Figure 21(a) shows that the ground-state energy $E_0(H_{\text{ferro}})$ converges towards Eq. (B7) as N increases. In other words, CCSD gives the exact ground-state energy in the thermodynamic limit. Figure 21(b) compares the three approximations $E_0^{\text{HF}}(H_{\text{ferro}})$ [cf. Eq. (B4)], $E_0^{\text{CI}}(H_{\text{ferro}})$ [76], and $E_0^{\text{CC}}(H_{\text{ferro}})$ in the limit $N \rightarrow \infty$. One sees that CISD fails to account for a significant part of the correlation energy around the critical point.

It is interesting to point out that the $N \rightarrow \infty$ solution (B7) can also be obtained via the Holstein-Primakoff transform [6,7]. Between the two approaches, the derivation based on Holstein-Primakoff transform is slightly easier compared to CCSD. On the other hand, one corollary from the CCSD approach is that we know that in the thermodynamic limit the ground state of H_{ferro} consists of only singles and doubles excitations, with the wave function taking the simple and compact form $e^{T^{\text{SD}}} |0\rangle$. This is an insight from coupled-cluster theory which is not immediately apparent from the Holstein-Primakoff approach.

APPENDIX C: WAVE FUNCTIONS OF VARIOUS APPROXIMATIONS IN J_z REPRESENTATION

The numerical diagonalization of the Hamiltonians (15) and (B1) was performed in the representation where the

operator J_z is diagonal. In this Appendix, we discuss the representations of Hartree-Fock, CISD, and CCSD wave functions in this basis. This allows us to compare these approximations with the energy eigenfunctions that are obtained numerically.

Denote $|m_z\rangle$ as the eigenvector of J_z , where $m_z = -N, -N+2, \dots, N$ is the projection quantum number in the z direction. Expressing $|m_z\rangle$ in the σ_i^z basis, one has

$$|m_z\rangle = \binom{N}{n_d}^{-\frac{1}{2}} \sum_{\{i_1, \dots, i_{n_d}\} \in \mathcal{M}} |i_1 \dots i_{n_d}\rangle, \quad (\text{C1})$$

where $n_d = (N - m_z)/2$ is the number of spins pointing down in $|m_z\rangle$, and $|i_1 \dots i_{n_d}\rangle$ denotes a Hartree-Fock state in which the spins with indices i_1, \dots, i_{n_d} are in the spinor state $\binom{0}{1}$ while the rest are in $\binom{1}{0}$. The symbol \mathcal{M} denotes all possible ways to choose n_d indices from N , and the binomial coefficient $\binom{N}{n_d}$ is to ensure normalization of $|m_z\rangle$. In the following, the expansion coefficients of a wave function $|\Psi\rangle$ in the basis $|m_z\rangle$ is obtained by computing the inner product $\langle m_z | \Psi \rangle$.

1. Hartree-Fock approximation

For the Hartree-Fock state $|0\rangle = \binom{\alpha}{\beta}^N$, one has

$$\langle m_z | 0 \rangle = \binom{N}{n_d}^{\frac{1}{2}} \alpha^{N-n_d} \beta^{n_d}. \quad (\text{C2})$$

2. CISD approximation

The CISD wave function is given by [7]

$$|\text{CI}\rangle = \left(\hat{x} + \hat{y} \sum_i \sigma_i^y + \hat{w} \sum_{i>j} \sigma_i^y \sigma_j^y \right) |0\rangle, \quad (\text{C3})$$

where $|0\rangle$ is as in Eq. (C2), and \hat{x} , \hat{y} , \hat{w} are determined by minimizing $\langle \text{CI} | H | \text{CI} \rangle$ subjected to $\langle \text{CI} | \text{CI} \rangle = 1$. The inner product is

$$\begin{aligned} \langle m_z | \text{CI} \rangle = & \mathcal{N}_{\text{CI}} \{ \hat{x} \alpha^{N-n_d} \beta^{n_d} \\ & + \hat{y} [n_d \alpha^{N-(n_d-1)} \beta^{n_d-1} - (N-n_d) \alpha^{N-(n_d+1)} \beta^{n_d+1}] \\ & + \frac{\hat{w}}{2} [n_d(n_d-1) \alpha^{N-(n_d-2)} \beta^{n_d-2} \\ & + (N-n_d)(N-n_d-1) \alpha^{N-(n_d+2)} \beta^{n_d+2} \\ & - 2n_d(N-n_d) \alpha^{N-n_d} \beta^{n_d}] \}, \end{aligned} \quad (\text{C4})$$

where $\mathcal{N}_{\text{CI}} = [\binom{N}{n_d}^{-1} (\hat{x}^2 + N\hat{y}^2 + \frac{N(N-1)}{2}\hat{w}^2)]^{-\frac{1}{2}}$. To avoid overflows when evaluating Eq. (C4) numerically, it is advisable to first group the $\binom{N}{n_d}$ in \mathcal{N}_{CI} together with the powers of α and β , and then sum up their exponents.

3. CCSD approximation

We write the normalized CCSD wave function as

$$|\text{CC}\rangle = \mathcal{N}_{\text{CC}} e^{-Nw} e^{T^{\text{SD}}} |0\rangle, \quad (\text{C5})$$

where $|0\rangle$ is as before, and $\mathcal{N}_{\text{CC}} = [2^{-N} \sum_{i=0}^N \binom{N}{i} e^{-w(N-2i)^2}]^{-\frac{1}{2}}$.

When n_d is even, one has

$$\begin{aligned} \langle m_z | \text{CC} \rangle = & \nu \mathcal{N}' \sum_{q=0}^{N-n_d} \sum_{r=0}^{n_d} (-1)^r \cos\{(\theta+y)[N-2(q+r)]\} \\ & \times \binom{N-n_d}{q} \binom{n_d}{r} e^{-\frac{w}{2}[N-2(q+r)]^2}, \end{aligned} \quad (\text{C6})$$

where $\mathcal{N}' = 2^{-N} \binom{N}{n_d}^{\frac{1}{2}} \mathcal{N}_{\text{CC}}$, the angle θ is given by $e^{i\theta} = \alpha + i\beta$, and

$$\nu = \begin{cases} +1 & \text{when } n_d = 0, 4, 8, \dots, \\ -1 & \text{when } n_d = 2, 6, 10, \dots \end{cases} \quad (\text{C7})$$

When n_d is odd, replace the cosine in Eq. (C6) by sine, and ν by

$$\tilde{\nu} = \begin{cases} +1 & \text{when } n_d = 1, 5, 9, \dots, \\ -1 & \text{when } n_d = 3, 7, 11, \dots \end{cases} \quad (\text{C8})$$

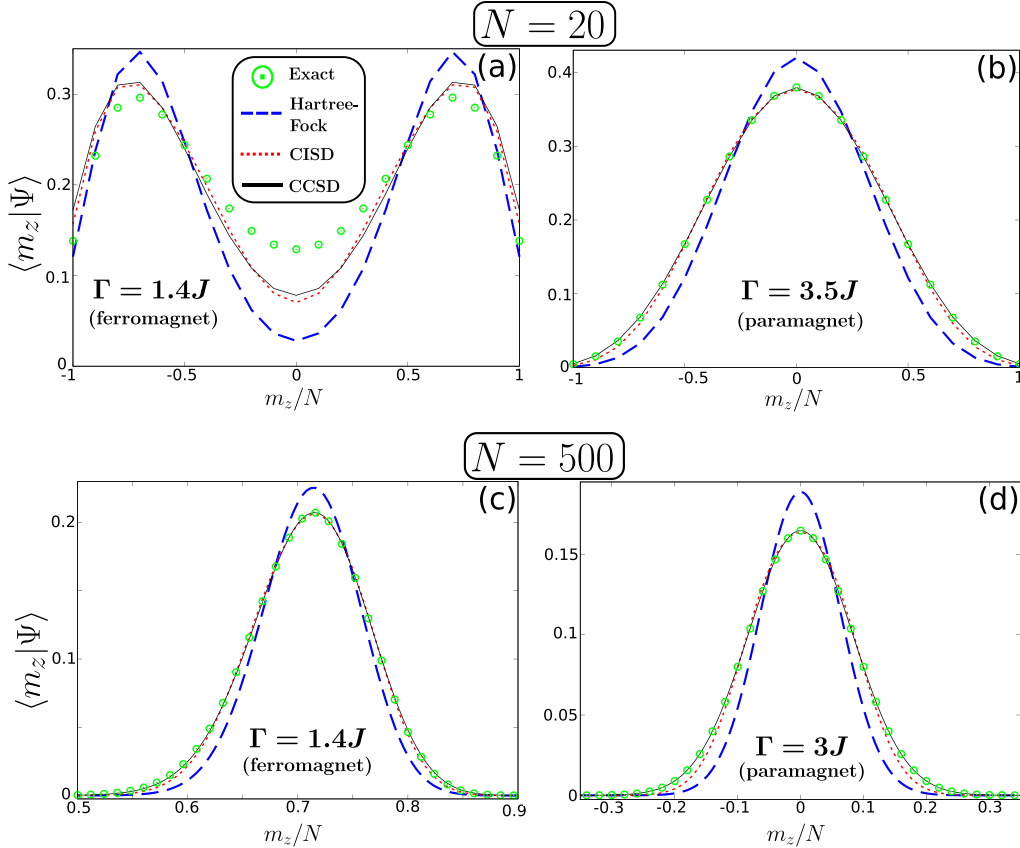


FIG. 22. Comparing the exact and approximated ground-state wave functions of the ferromagnetic model H_{ferro} . The wave functions are represented using the eigenvectors $|m_z\rangle$ of the operator J_z . (a), (b) $N = 20$. (c), (d) $N = 500$. (a), (c) Ferromagnetic regime. (b), (d) Paramagnetic regime. The symbols shown in (a) apply to all panels. The CCSD results for $N = 20$ are obtained using Eqs. (C6) to (C8), while those for $N = 500$ using Eq. (C11). Overall, CCSD (black solid curve) gives the closest approximation to the exact ground state (green circles).

Although Eq. (C6) is exact, it is difficult to evaluate accurately when N is large due to numerical overflow. To avoid that, note that before integrating out the random field m , one has

$$\langle m_z | \text{CC} \rangle = \mathcal{N}_{\text{CC}} \left[\binom{N}{n_d} \left(\frac{N}{2\pi} \right) \right]^{\frac{1}{2}} \int dm \exp[-Nf(m)], \quad (\text{C9})$$

where

$$f(m) = \frac{1}{2}m^2 - \left(1 - \frac{n_d}{N}\right) \ln(\alpha \cos t - \beta \sin t) - \left(\frac{n_d}{N}\right) \ln(\beta \cos t + \alpha \sin t) \quad (\text{C10})$$

and $t = y + m\sqrt{Nw}$. When N is large, the integral (C9) can be approximated by the method of steepest descent

$$\langle m_z | \text{CC} \rangle \approx \mathcal{N}_{\text{CC}} \left(\frac{N}{n_d} \right)^{\frac{1}{2}} |f''(m_0)|^{-\frac{1}{2}} e^{-Nf(m_0)}, \quad (\text{C11})$$

where m_0 is the solution of the saddle-point equation $f'(m_0) = 0$.

4. Application to the ferromagnetic model

Let us apply the above results to the ferromagnetic model (B1). Each panel in Fig. 22 compares the Hartree-Fock (blue dashed), CISD (red dotted), and CCSD (black solid) wave functions with the exact ground state obtained via diagonalization (green circles). Figures 22(a) and 22(b) show the results for a small system size of $N = 20$, while Figs. 22(c) and 22(d) show for a larger one of $N = 500$. Figures 22(a) and 22(c) show the situation in the ferromagnetic regime, while Figs. 22(b) and 22(d) that in the paramagnetic one. Overall, one sees that both CISD and CCSD are quite accurate, although at the visual level CCSD performs slightly better than CISD. The sole exception is Fig. 22(a) ($N = 20$, ferromagnetic regime) where all three approximations deviate rather significantly from the exact result. This highlights the difficulty of attaining accurate approximations in the ordered phase when the system size is small.

-
- [1] F. Zhang, N. Gomes, Y. Yao, P. P. Orth, and T. Iadecola, *Phys. Rev. B* **104**, 075159 (2021).
 - [2] Y. Seki, Y. Matsuzaki, and S. Kawabata, *J. Phys. Soc. Jpn.* **90**, 054002 (2021).
 - [3] T. Albash and D. A. Lidar, *Rev. Mod. Phys.* **90**, 015002 (2018).
 - [4] S. H. Tekur, U. T. Bhosale, and M. S. Santhanam, *Phys. Rev. B* **98**, 104305 (2018).
 - [5] W. Beugeling, A. Bäcker, R. Moessner, and M. Haque, *Phys. Rev. E* **98**, 022204 (2018).
 - [6] S. Dusuel and J. Vidal, *Phys. Rev. B* **71**, 224420 (2005).
 - [7] Y. W. Koh, *Phys. Rev. B* **93**, 134202 (2016).
 - [8] Technically speaking, the term “classical energy landscape” should more appropriately be referred to as “mean-field energy landscape” or “semiclassical energy landscape.” However, as the former nomenclature sounds more intuitive and is not as heavy as the latter two, we chose to use the former.
 - [9] A. J. Bray and M. A. Moore, *J. Phys. C: Solid State Phys.* **13**, L655 (1980).
 - [10] T. Yamamoto and H. Ishii, *J. Phys. C: Solid State Phys.* **20**, 6053 (1987).
 - [11] D. Thirumalai, Q. Li, and T. R. Kirkpatrick, *J. Phys. A: Math. Gen.* **22**, 3339 (1989).
 - [12] P. Ray, B. K. Chakrabarti, and A. Chakrabarti, *Phys. Rev. B* **39**, 11828 (1989).
 - [13] G. Büttner and K. D. Usadel, *Phys. Rev. B* **41**, 428 (1990).
 - [14] Y. Y. Goldschmidt and P. Y. Lai, *Phys. Rev. Lett.* **64**, 2467 (1990).
 - [15] K. D. Usadel, G. Büttner, and T. K. Kopeć, *Phys. Rev. B* **44**, 12583 (1991).
 - [16] T. K. Kopeć, *Phys. Rev. B* **50**, 9963 (1994).
 - [17] N. Read, S. Sachdev, and J. Ye, *Phys. Rev. B* **52**, 384 (1995).
 - [18] V. Dobrosavljević and D. Thirumalai, *J. Phys. A: Math. Gen.* **23**, L767 (1990).
 - [19] Y. Y. Goldschmidt, *Phys. Rev. B* **41**, 4858(R) (1990).
 - [20] L. De Cesare, K. Lukierska-Walasek, I. Rabuffo, and K. Walasek, *J. Phys. A: Math. Gen.* **29**, 1605 (1996).
 - [21] T. Obuchi, H. Nishimori, and D. Sherrington, *J. Phys. Soc. Jpn.* **76**, 054002 (2007).
 - [22] J. Miller and D. A. Huse, *Phys. Rev. Lett.* **70**, 3147 (1993).
 - [23] D. R. Grempel and M. J. Rozenberg, *Phys. Rev. Lett.* **80**, 389 (1998).
 - [24] M. J. Rozenberg and D. R. Grempel, *Phys. Rev. Lett.* **81**, 2550 (1998).
 - [25] L. Arrachea and M. J. Rozenberg, *Phys. Rev. Lett.* **86**, 5172 (2001).
 - [26] H. Ishii and T. Yamamoto, *J. Phys. C: Solid State Phys.* **18**, 6225 (1985).
 - [27] L. De Cesare, K. Lukierska Walasek, and K. Walasek, *Phys. Rev. B* **45**, 8127 (1992).
 - [28] G. Biroli and L. F. Cugliandolo, *Phys. Rev. B* **64**, 014206 (2001).
 - [29] A. Gubin and L. F. Santos, *Am. J. Phys.* **80**, 246 (2012).
 - [30] J. Zakrzewski, *Entropy* **25**, 491 (2023).
 - [31] W. G. Brown, L. F. Santos, D. J. Starling, and L. Viola, *Phys. Rev. E* **77**, 021106 (2008).
 - [32] B. Georgeot and D. L. Shepelyansky, *Phys. Rev. E* **62**, 3504 (2000).
 - [33] B. Georgeot and D. L. Shepelyansky, *Phys. Rev. E* **62**, 6366 (2000).
 - [34] B. Georgeot and D. L. Shepelyansky, *Phys. Rev. Lett.* **81**, 5129 (1998).
 - [35] S. Bera, K. Y. Venkata Lokesh, and S. Banerjee, *Phys. Rev. Lett.* **128**, 115302 (2022).
 - [36] M. Winer, R. Barney, C. L. Baldwin, V. Galitski, and B. Swingle, *J. High Energy Phys.* **09** (2022) 032.
 - [37] C. R. Laumann, A. Pal, and A. Scardicchio, *Phys. Rev. Lett.* **113**, 200405 (2014).
 - [38] C. L. Baldwin, C. R. Laumann, A. Pal, and A. Scardicchio, *Phys. Rev. Lett.* **118**, 127201 (2017).
 - [39] S. Mukherjee, S. Nag, and A. Garg, *Phys. Rev. B* **97**, 144202 (2018).
 - [40] J. Z. Imbrie, *Phys. Rev. Lett.* **117**, 027201 (2016).

- [41] J. A. Kjäll, J. H. Bardarson, and F. Pollmann, *Phys. Rev. Lett.* **113**, 107204 (2014).
- [42] M. Lee, T. R. Look, S. P. Lim, and D. N. Sheng, *Phys. Rev. B* **96**, 075146 (2017).
- [43] G. Biroli and M. Tarzia, *Phys. Rev. B* **102**, 064211 (2020).
- [44] M. Tarzia, *Phys. Rev. B* **102**, 014208 (2020).
- [45] L. Herviou, J. H. Bardarson, and N. Regnault, *Phys. Rev. B* **103**, 134207 (2021).
- [46] M. H. Amin, *Phys. Rev. A* **92**, 052323 (2015).
- [47] S. Boixo, V. N. Smelyanskiy, A. Shabani, S. V. Isakov, M. Dykman, V. S. Denchev, M. H. Amin, A. Y. Smirnov, M. Mohseni, and H. Neven, *Nat. Commun.* **7**, 10327 (2016).
- [48] V. S. Denchev, S. Boixo, S. V. Isakov, N. Ding, R. Babbush, V. N. Smelyanskiy, J. M. Martinis, and H. Neven, *Phys. Rev. X* **6**, 031015 (2016).
- [49] F. Jensen, *Introduction to Computational Chemistry* (Wiley, Chichester, UK, 2007).
- [50] R. J. Bartlett and M. Musial, *Rev. Mod. Phys.* **79**, 291 (2007).
- [51] The term excitation, when used in the context of coupled-cluster theory, should be understood in terms of correlation effects, and not as the energy difference between two energy eigenstates.
- [52] J. P. F. LeBlanc, A. E. Antipov, F. Becca, I. W. Bulik, G. K.-L. Chan, C. M. Chung, Y. Deng, M. Ferrero, T. M. Henderson, C. A. Jimenez-Hoyos, E. Kozik, X. W. Liu, A. J. Millis, N. V. Prokofev, M. Qin, G. E. Scuseria, H. Shi, B. V. Svistunov, L. F. Tocchio *et al.*, *Phys. Rev. X* **5**, 041041 (2015).
- [53] M. Roger and J. H. Hetherington, *Phys. Rev. B* **41**, 200 (1990).
- [54] R. F. Bishop, J. B. Parkinson, and Y. Xian, *Phys. Rev. B* **44**, 9425 (1991); **46**, 880 (1992).
- [55] B. Miguel and J.-P. Malrieu, *Phys. Rev. B* **54**, 1652 (1996).
- [56] D. J. J. Farnell, K. A. Gernoth, and R. F. Bishop, *Phys. Rev. B* **64**, 172409 (2001).
- [57] S. E. Krüger, R. Darradi, J. Richter, and D. J. J. Farnell, *Phys. Rev. B* **73**, 094404 (2006).
- [58] R. Darradi, O. Derzhko, R. Zinke, J. Schulenburg, S. E. Krüger, and J. Richter, *Phys. Rev. B* **78**, 214415 (2008).
- [59] J. Richter, R. Darradi, J. Schulenburg, D. J. J. Farnell, and H. Rosner, *Phys. Rev. B* **81**, 174429 (2010).
- [60] O. Götze, D. J. J. Farnell, R. F. Bishop, P. H. Y. Li, and J. Richter, *Phys. Rev. B* **84**, 224428 (2011).
- [61] O. Götze and J. Richter, *Phys. Rev. B* **91**, 104402 (2015).
- [62] S. Hirata, *J. Phys. Chem. A* **107**, 9887 (2003).
- [63] Y. Seki and H. Nishimori, *Phys. Rev. E* **85**, 051112 (2012).
- [64] The more accurate CCSD wave function (C11) gives a closer correspondence with the energy eigenfunction. The Hartree-Fock wave function, however, is simpler and sufficient to illustrate our point.
- [65] Y. Q. Ma and C. D. Gong, *Phys. Rev. B* **48**, 12778 (1993).
- [66] Y. Q. Ma, Y. M. Zhang, Y. G. Ma, and C. D. Gong, *Phys. Rev. E* **47**, 3985 (1993).
- [67] H. Nishimori and Y. Nonomura, *J. Phys. Soc. Jpn.* **65**, 3780 (1996).
- [68] D. J. Amit, *Modeling Brain Function: The World of Attractor Neural Networks* (Cambridge University Press, Cambridge, 1989).
- [69] P. Reberntrost, T. R. Bromley, C. Weedbrook, and S. Lloyd, *Phys. Rev. A* **98**, 042308 (2018).
- [70] G. Liu, W. P. Ma, H. Cao, and L. D. Lyu, *Laser Phys. Lett.* **17**, 045201 (2020).
- [71] N. E. Miller and S. Mukhopadhyay, *Sci. Rep.* **11**, 23391 (2021).
- [72] The patterns are $\xi^1 = (1, 1, 1, 1, 1, 1, 1, 1, 1, -1, -1, -1, 1, 1, 1)$, $\xi^2 = (1, 1, 1, 1, 1, 1, -1, -1, -1, -1, 1, 1, 1, 1, 1)$, $\xi^3 = (1, 1, 1, -1, -1, -1, 1, 1, 1, 1, 1, 1, -1, -1, 1)$, and $\xi^4 = (1, -1, -1, 1, 1, 1, 1, 1, 1, 1, 1, 1, -1, -1, -1)$.
- [73] We used $\omega = (1, -1, -1, 1, 1, 1, 1, 1, 1, 0, 1, 1, -1, -1, -1)$ and $p = (0, 0, -1, -1, 2, 2, -1, -1, -1, -1, -1, -1, 1, 1, -1)$.
- [74] Y. Qiu, Spectra, <https://spectralib.org>. Using this package, we outputted the lowest 1400 eigenvalues of H_{Hop} , and checked that those that we need, E_0 to E_{450} , are converged.
- [75] D. J. Rowe, *Rev. Mod. Phys.* **40**, 153 (1968).
- [76] The analytical expression for $E_0^{\text{CI}}(H_{\text{ferro}})$ in the limit $N \rightarrow \infty$ is given by Eq. (A6) in Ref. [7].